A high-resolution Petrov–Galerkin method for the convection–diffusion–reaction problem. Part II—A multidimensional extension

Prashanth Nadukandi [a,b,*], Eugenio Oñate [a,b], Julio García [a,b]

[a] Centre Internacional de Mètodes Numèrics en Enginyeria (CIMNE), Edifici C1, Campus Norte UPC, C/ Gran Capitán S/N, 08034 Barcelona, Spain
[b] Universitat Politècnica de Catalunya (UPC), Edifici C1, C/ Jordi Girona 1-3, 08034 Barcelona, Spain

A B S T R A C T

A multidimensional extension of the HRPG method (doi:10.1016/j.cma.2009.10.009) using the lowest order block finite elements is presented. First, we design a nondimensional element number that quan-tifies the characteristic layers which are found only in higher dimensions. This is done by matching the width of the characteristic layers to the width of the parabolic layers found for a fictitious 1D reaction–diffusion problem. The nondimensional element number is then defined using this fictitious reaction coefficient, the diffusion coefficient and an appropriate element size. Next, we introduce anisotropic ele-ment length vectors $\mathbf{l}^i$ and the stabilization parameters α^i, β^i are calculated along these $\mathbf{l}^i$. Except for the modification to include the new dimensionless number that quantifies the characteristic layers, the def-initions of α^i, β^i are a direct extension of their counterparts in 1D. Using α^i, β^i and $\mathbf{l}^i$, objective character-istic tensors associated with the HRPG method are defined. The numerical artifacts across the characteristic layers are manifested as the Gibbs phenomenon. Hence, we treat them just like the artifacts formed across the parabolic layers in the reaction-dominant case. Several 2D examples are presented that support the design objective—stabilization with high-resolution.

1. Introduction

It is well known that the solution to the singularly perturbed convection–diffusion–reaction problem may develop two types of layers—exponential and parabolic layers. The first-order derivatives in the direction perpendicular to the exponential layers have a magnitude of $O(1/k)$. Here k is the diffusion coefficient which may take arbitrarily small values. For the parabolic layers these derivatives have a magnitude of $O\left(1/\sqrt{k}\right)$ and hence they are of larger width than the exponential layers [1]. The exponential layers are usually found in the convection-dominant cases near the outflow boundary or close to the regions where the source term is non regular. Parabolic layers are found in the reaction-dominant cases near the boundary or close to the regions where the source term is non regular and in the convection-dominated cases across the characteristic lines of the solution.

The numerical artifacts observed in the solution of the singularly perturbed CDR problem using the Bubnov–Galerkin FEM (BG-FEM) can be broadly classified into three groups: (a) spurious global oscillations, (b) Gibbs phenomenon and (c) numerical dispersion. The spurious global oscillations are typically found in the solution of the stationary problem in the presence of exponential layers. The Gibbs phenomenon is a spurious oscillation that occurs when using a truncated Fourier series or other eigen function series at a simple discontinuity. It is characterized by an initial overshoot and then a pattern of undershoot-overshoot oscillations that decrease in amplitude further from the discontinuity. Unlike the global instability, the Gibbs phenomenon does not amplify arbitrarily as $k \to 0$. A classical example is the L^2 projection of a given discontinuous function in any subspace. Typical examples where we can observe the Gibbs phenomenon are the BG-FEM solutions (a) of the reaction-dominant stationary CDR problem, (b) across the characteristic lines in the convection-dominant stationary CDR problem and (c) of the transient CDR problem using very small time steps with a discontinuous initial solution. Thus, the Gibbs phenomenon is usually observed in the presence of parabolic layers. Numerical dispersion is an artifact found in the solution of the transient CDR problem and is a characteristic feature of the spatial discretization. It occurs as the wave numbers in the amplitude spectra of the initial solution travel with phase and group velocities distinct from the one governed by the physical dispersion relation.

Several stabilized methods were proposed to control this global instability [2–14]. A thorough comparison of some of these methods can be found in [15]. Several shock-capturing nonlinear Petrov–Galerkin methods were proposed to control the Gibbs oscillations observed across characteristic internal/boundary layers for the convection–diffusion problem [16–28]. A thorough

* Corresponding author. Address: Centre Internacional de Mètodes Numèrics en Enginyeria (CIMNE), Edifici C1, Campus Norte UPC, C/ Gran Capitán S/N, 08034 Barcelona, Spain. Tel.: +34 93 401 0795; fax: +34 93 401 6517.
E-mail addresses: npras@cimne.upc.edu, nadukandi@gmail.com (P. Nadukandi).

review, comparison and state of the art of these and several other shock-capturing methods for the convection–diffusion equations, therein named as *spurious oscillations at layers diminishing* methods, was done in [29]. Reactive terms were not considered in the design of these methods and hence they fail to control the localized oscillations in the presence of these terms. Exceptions to this are the CAU method [18], the methods presented in [22,24] and those that take the CAU method as the starting point [20,25,26]. Nevertheless the expressions for the stabilization parameters therein were never optimized for reactive instability and often the solutions are over-diffusive in these cases.

Several methods were built upon the existing frameworks of globally stabilized methods to control the Gibbs phenomenon in the reaction dominant cases [30–43]. Generally the homogeneous steady CDR problem in 1D has two fundamental solutions. Likewise, the characteristic equation associated with linear stabilized methods which result in compact stencils are quadratic and hence have two solutions. Thus in principle using two stabilization parameters (independent of the boundary conditions) linear stabilized methods which result in compact stencils can be designed to be nodally exact in 1D. Following this line several 'two-parameter methods' viz. [31,33,40] were designed to be nodally exact for the stationary problem in 1D.

Some methods were proposed in [44,45] in order to control the Gibbs phenomenon see in the initial stages of the transient evolution of a discontinuous function using very small time steps. Control over the dispersive oscillations for the transient convection–diffusion problem via linear Petrov–Galerkin methods were discussed in [46] and using space–time finite elements in [47]. As for the linear methods, optimizing the expressions of the stabilization parameters to attain monotonicity will lead to solutions that are at most first-order accurate.

It was pointed out in [48] that in 1D the performance of the DC [17] and CD [21] methods are similar to that of the SUPG method. This is due to the fact that in 1D $\mathbf{u}^{\parallel} = \mathbf{u}$ (see Table 1) and here the notion of crosswind directions does not exist. On the other hand the nonlinear shock-capturing term introduced by the CAU method are retained in 1D and thus in principle are able to control the Gibbs and dispersive oscillations. This feature does carry over to all the methods that have the shock-capturing term similar to that in the CAU method viz. the methods presented in [20,22,24–26]. Unfortunately as pointed out in [29] and [48, Section 5.7.1], these methods are often over diffusive.

This paper is a continuation of [48] wherein a nonlinear high-resolution Petrov–Galerkin (HRPG) method was presented for the convection–diffusion–reaction (CDR) problem in 1D. The structure of the method in 1D is identical to the consistent approximate upwind (CAU) Petrov–Galerkin method [18] except for the definition of the stabilization parameters. The prefix 'high-resolution' is used here in the sense popularized by Harten in the finite-difference and finite-volume communities, i.e. second-order accuracy for smooth/regular regimes and good shock-capturing in non regular regimes. In this paper we develop an extension to multi dimensions of the HRPG method for the singularly perturbed CDR problem using the lowest order block finite elements. By blocks we mean Cartesian product of intervals and by lowest order we refer to multi-linear finite element (FE) interpolation on these blocks.

The outline of this paper is as follows. In Section 2 we present the statement of the CDR problem in both the strong and the weak forms. The statement of the HRPG method is also given here in both the semi-discrete and fully-discrete forms. In Section 3 we explain concisely the origins and the motivation behind the procedure to calculate the stabilization parameters of the HRPG method as proposed for the 1D CDR problem in [48]. In Section 4 we discuss the numerical artifacts found across the characteristic layers which are manifested as the Gibbs phenomenon and comment on the strategy used to treat them. In Section 5 we design a nondimensional element number that quantifies the characteristic internal/boundary layers. Anisotropic element length vectors $\mathbf{l}^i$ are introduced in Section 6 and using them objective characteristic tensors $\mathbf{h}$ and $\mathbf{H}$ associated with the HRPG method are defined. The stabilization parameters α^i, β^i used in the definition of $\mathbf{h}$, $\mathbf{H}$ are defined in Section 7 by a direct extension of their respective expressions in 1D. The definitions of β^i are updated to include the new dimensionless number introduced in Section 5. In Box 2 we summarize the HRPG method in multi dimensions. Several numerical examples are presented in Section 8 that throws light on the performance of the proposed method for a wide range of problem data. Finally we arrive at some conclusions and outlook in Section 9.

Table 1
Perturbations associated with Petrov–Galerkin methods [48, Table 1].

Method	Perturbation (p_h)	Remarks
SUPG [2]	$\tau\mathbf{u}\cdot\nabla w_h$	
MH [16]	C_i^e	$C_i^e \in \left\{-\frac{1}{3}, \frac{2}{3}\right\},\ i=1,2,3$ $\sum_i C_i^e = 0$
DC [17]	$\tau_1\mathbf{u}\cdot\nabla w_h + \tau_2\mathbf{u}^{\parallel}\cdot\nabla w_h$	$\mathbf{u}^{\parallel} := \frac{\mathbf{u}\cdot\nabla\phi_h}{\lvert\nabla\phi_h\rvert^2}\nabla\phi_h$
CAU [18], CCAU [20]	$\tau_1\mathbf{u}\cdot\nabla w_h + \tau_2\mathbf{u}^{r}\cdot\nabla w_h$	$\mathbf{u}^{r} := \frac{R(\phi_h)}{\lvert\nabla\phi_h\rvert^2}\nabla\phi_h$
CD [21]	$\tau_1\mathbf{u}\cdot\nabla w_h + \alpha_2\ell\nabla w_h\cdot[\mathbf{I}-\widehat{\mathbf{u}}\otimes\widehat{\mathbf{u}}]\cdot\widehat{\mathbf{u}}^{r}$	$\widehat{\mathbf{u}} := \frac{\mathbf{u}}{\lvert\mathbf{u}\rvert}$, $\widehat{\mathbf{u}}^{r} := \frac{\mathbf{u}^{r}}{\lvert\mathbf{u}^{r}\rvert}$ $\widehat{\mathbf{u}}^{r} = \frac{\operatorname{sgn}[R(\phi_h)]}{\lvert\nabla\phi_h\rvert}\nabla\phi_h$
SAUPG [25], Mod.CAU [21]	$\tau[\lambda\mathbf{u} + (1-\lambda)\mathbf{u}^{r}]\cdot\nabla w_h$	λ is a smoothness measure
FIC [14]	$\mathbf{h}^{\text{fic}}\cdot\nabla w_h$	Here $\mathbf{h}^{\text{fic}}$ is a characteristic length vector which may be defined in a linear or nonlinear fashion
HRPG [48]	$[\mathbf{h}+\mathbf{H}\cdot\hat{\mathbf{u}}^{r}]\cdot\nabla w_h$	$\mathbf{h}$, $\mathbf{H}$ are frame-independent linear characteristic length tensors based on the element geometry (see Section 6)

2. Problem statement

The statement of the multidimensional CDR problem in the strong form is,

$$R(\phi) := \frac{\partial\phi}{\partial t} + \mathbf{u}\cdot\nabla\phi - \nabla\cdot(k\nabla\phi) + s\phi - f(\mathbf{x}) = 0 \quad \text{in } \Omega \tag{1a}$$

$$\phi(\mathbf{x}, t=0) = \phi_0(\mathbf{x}) \quad \text{in } \Omega \tag{1b}$$

$$\phi = \phi^p \quad \text{on } \Gamma_{\mathrm{D}} \tag{1c}$$

$$k\nabla\phi\cdot\mathbf{n} + g^p = 0 \quad \text{on } \Gamma_{\mathrm{N}} \tag{1d}$$

where $\mathbf{u}$ is the convection velocity, k and s are the diffusion and reaction coefficients respectively, $f(\mathbf{x})$ is the source, $\phi_0(\mathbf{x})$ is the initial solution, ϕ^p and g^p are the prescribed values of ϕ and the diffusive flux at the Dirichlet and Neumann boundaries respectively and $\mathbf{n}$ is the normal to the boundary.

For the solution of the problem (1) we introduce the following space of functions:

$$V := \{w : w \in H^1(\Omega) \quad \text{and} \quad w = \phi^p \quad \text{on } \Gamma_{\mathrm{D}}\} \tag{2a}$$

$$V_0 := \{w : w \in H^1(\Omega) \quad \text{and} \quad w = 0 \quad \text{on } \Gamma_{\mathrm{D}}\} \tag{2b}$$

where $H^m(\Omega)$ is the usual Sobolev space of functions with mth derivatives square integrable. The weak form of the problem (1)

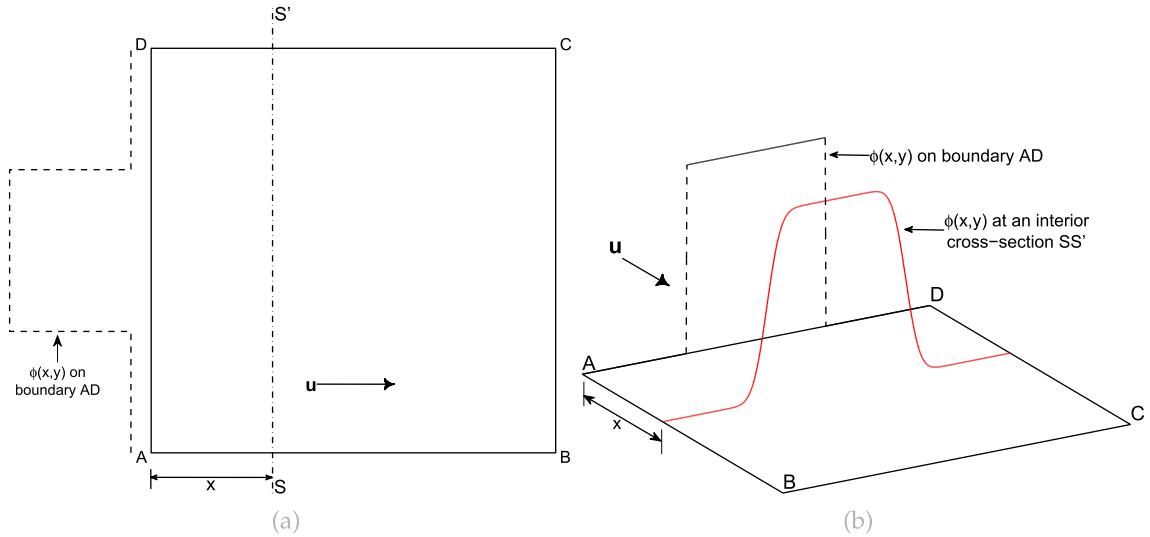

Fig. 1. A singularly perturbed convection–diffusion problem. (a) The problem domain *ABCD* and boundary conditions; (b) The solution about a cross-section *SS'* located at a distance x from the boundary AD.

can be expressed as follows: find $\phi : [0,T] \mapsto V$ such that $\forall w \in V_0$ we have,

$$\int_\Omega w \frac{\partial \phi}{\partial t}\, \mathrm{d}\Omega + a(w,\phi) = l(w) \tag{3a}$$

$$a(w,\phi) := \int_\Omega w[\mathbf{u}\cdot\nabla\phi + s\phi] + k\nabla w\cdot\nabla\phi\, \mathrm{d}\Omega \tag{3b}$$

$$l(w) := \int_\Omega wf(x)\, \mathrm{d}\Omega - \int_{\Gamma_N} wg^p\, \mathrm{d}\Gamma_N \tag{3c}$$

Let $V^h \subset V$ be a subspace obtained via any appropriate discretization with h being the discretization size parameter. The statement of the Galerkin method applied to the weak form of the problem (3) is: find $\phi_h : [0,T] \mapsto V^h$ such that $\forall w_h \in V_0^h$ we have,

$$\int_\Omega w_h \frac{\partial \phi_h}{\partial t}\, \mathrm{d}\Omega + a(w_h,\phi_h) = l(w_h) \tag{4}$$

Consider a partition of the domain Ω generated by a regular family of elements K. We follow [2] to describe a certain class of Petrov–Galerkin methods which account for weights that are discontinuous across element boundaries. The perturbed weighting function is written as $\widetilde{w}_h = w_h + p_h$, where p_h is the perturbation that account for the discontinuities. The statement of these class of Petrov–Galerkin methods is as follows: find $\phi_h : [0,T] \mapsto V^h$ such that $\forall w_h \in V_0^h$ we have,

$$\int_\Omega w_h \frac{\partial \phi_h}{\partial t}\, \mathrm{d}\Omega + a(w_h,\phi_h) + \sum_K \int_K p_h R(\phi_h)\, \mathrm{d}\Omega = l(w_h) \tag{5}$$

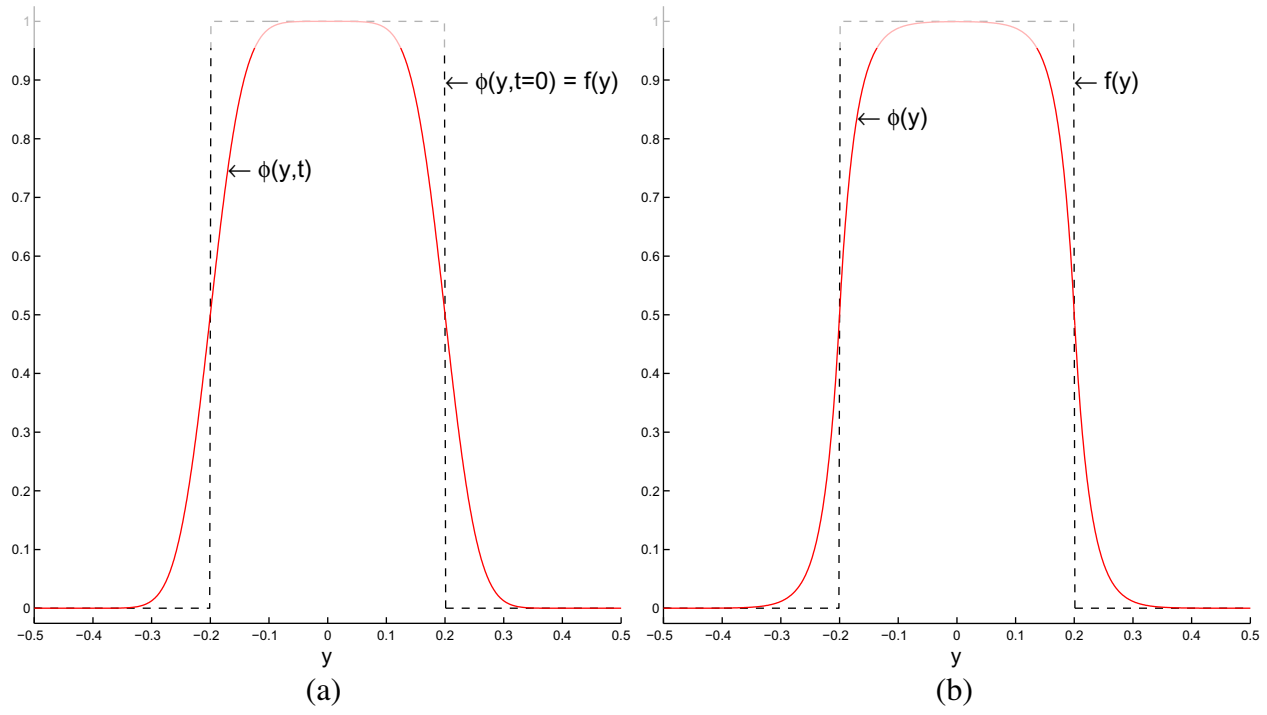

Fig. 2. Parabolic layers in the solution of: (a) the heat equation given by Eq. (24) using $k = 0.01$ and $t = 0.1$; (b) the diffusion–reaction problem given by Eq. (26) using $k = 0.01$ and $s = 10\sqrt{2}$.

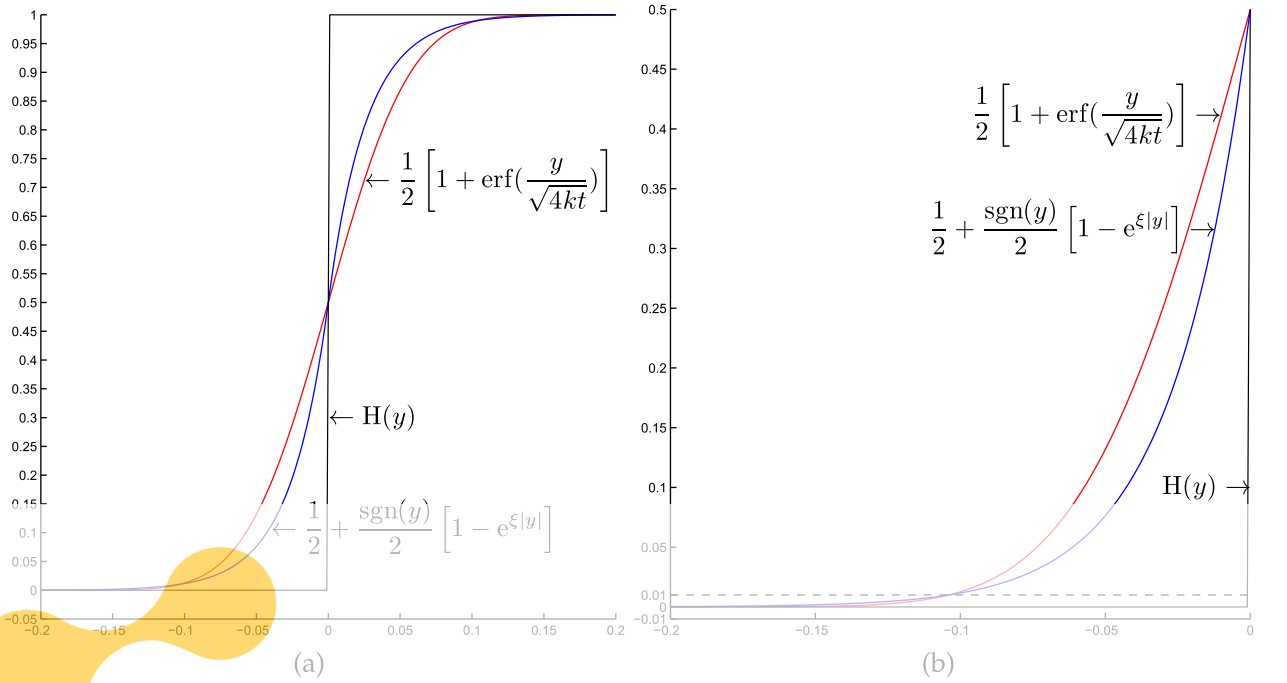

Fig. 3. Matching the layers in the solution of the heat equation and the diffusion–reaction problem. (a) plot domain: $[-0.2, 0.2]$, $k = 0.01$, $t = 0.1$ and $s := \left(\sqrt{2}/t\right) = 10\sqrt{2}$; (b) plot domain: $[-0.2, 0]$, the two solutions always meet at a value equal to 0.01.

The form of Eq. (5) can also be derived using the finite calculus (FIC) approach by expressing the balance equation in a domain of finite size and retaining higher order terms [14,49]. The HRPG method, whose design in 1D was presented in [48], is defined as Eq. (5) along with the following definition of p_h:

$$\mathbf{u}^r := \frac{R(\phi_h)}{|\nabla\phi_h|^2}\nabla\phi_h; \quad \Rightarrow \hat{\mathbf{u}}^r := \frac{\mathbf{u}^r}{|\mathbf{u}^r|} = \frac{\mathrm{sgn}[R(\phi_h)]}{|\nabla\phi_h|}\nabla\phi_h \tag{6a}$$

$$p_h := [\mathbf{h} + \mathbf{H}\cdot\hat{\mathbf{u}}^r]\cdot\nabla w_h = (\mathbf{h}\cdot\nabla w_h) + \frac{\mathrm{sgn}[R(\phi_h)]}{|\nabla\phi_h|}(\nabla w_h\cdot\mathbf{H}\cdot\nabla\phi_h) \tag{6b}$$

where 'sgn' represents the *signum* function that returns the sign of its argument, $\mathbf{h}$ and $\mathbf{H}$ are frame-independent linear *characteristic length* tensors of first and second order, respectively. The role of these tensors is to allow the treatment of the element anisotropy. We refer to Table 1 for a comparison of the HRPG method with the SUPG[2], FIC[14] and some of the existing shock-capturing methods.

Remark 1. From Eq. (6) and Table 1 the HRPG method could be understood as the combination of upwinding plus a nonlinear discontinuity-capturing operator. The distinction is that in general the upwinding provided by $\mathbf{h}$ is not streamline and the discontinuity-capturing provided by $\mathbf{H}\cdot\hat{\mathbf{u}}^r$ is neither isotropic nor purely crosswind. Of course, setting $\mathbf{h} := \tau\mathbf{u}$ and $\mathbf{H} := (\beta\ell)[\mathbf{I} - \hat{\mathbf{u}}\otimes\hat{\mathbf{u}}]$ one would recover (except for the definitions of the stabilization parameters) the CAU and the CD methods respectively. Note that one may arrive at the HRPG method via the FIC equations wherein the characteristic length is defined as $\mathbf{h}^{\mathrm{fic}} := \mathbf{h} + \mathbf{H}\cdot\hat{\mathbf{u}}^r$. From this point of view the HRPG method can be presented as 'FIC-based'.

Using the generalized trapezoidal method for integrating the semi-discrete Eq. (5) from t^n to $t^{n+1} = t^n + \Delta t$ and taking p_h as defined in Eq. (6) we get,

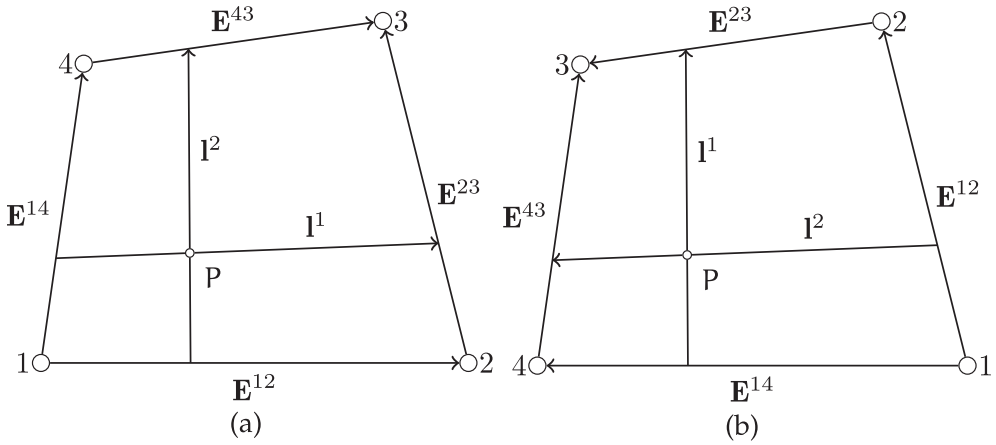

Fig. 4. Anisotropic element length vectors $\mathbf{l}^i$ obtained at any arbitrary point $P(\tilde{x}_1, \tilde{x}_2)$ within a 2D bilinear block finite element. The sub-figures (a) and (b) illustrate $\mathbf{l}^i$ obtained for two admissible global node numbering permutations.

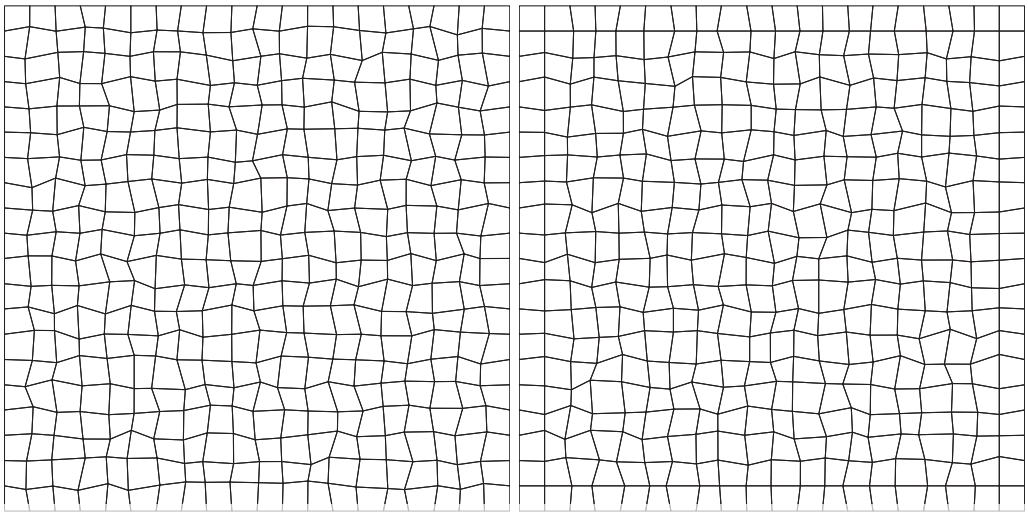

Fig. 5. Unstructured 20 × 20 meshes made of bilinear block finite elements. (a) Type I: all internal nodes of the mesh are perturbed using $\delta^* = 0.2$. (b) Type II: the perturbation perpendicular to the boundary was set to zero for the boundary-adjacent nodes of the mesh. For the rest of the cases $\delta^* = 0.2$ was chosen.

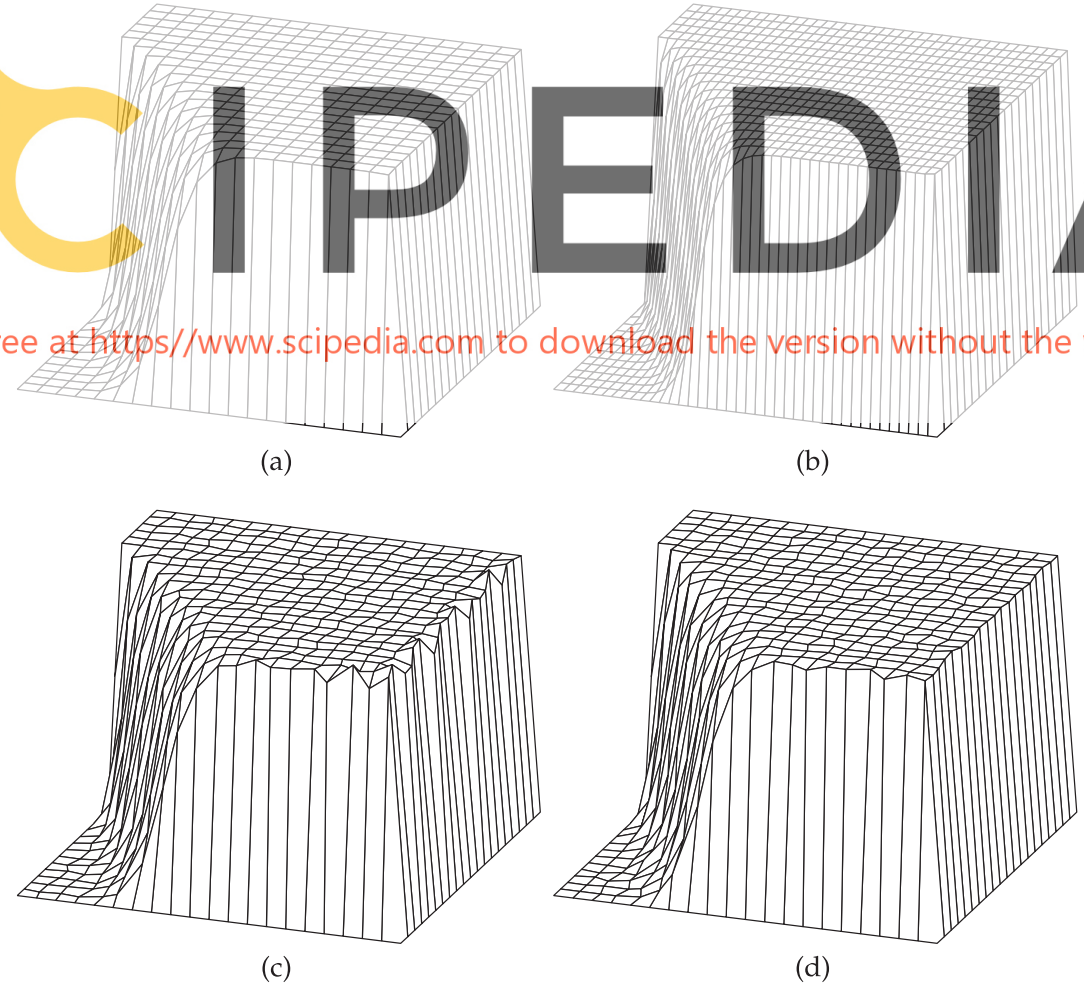

Fig. 6. Example 1, advection skew to the mesh. The solution of the HRPG method viewed at (20°,20°) and using (a) a structured 20 × 20 mesh, (b) a structured 40 × 20 mesh, (c) an unstructured (Type I) 20 × 20 mesh, (d) an unstructured (Type II) 20 × 20 mesh.

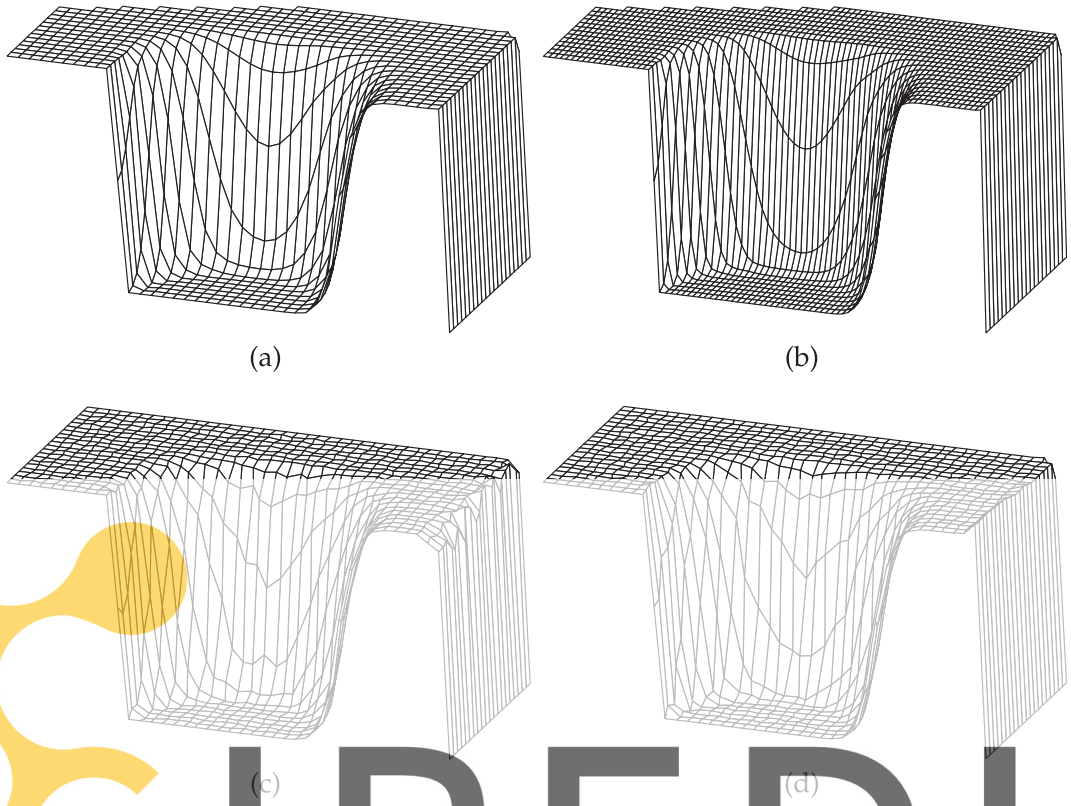

Fig. 7. Example 2, nonuniform rotational advection. The solution of the HRPG method viewed at (20°, 20°) and using (a) a structured 40×20 mesh, (b) a structured 80×20 mesh, (c) an unstructured (Type I) 40×20 mesh, (d) an unstructured (Type II) 40×20 mesh.

$$\int_\Omega w_h \frac{\phi_h^{n+\theta} - \phi_h^n}{\theta \Delta t}\, \mathrm{d}\Omega + a(w_h, \phi_h^{n+\theta}) + \sum_K \int_K (\mathbf{h} \cdot \nabla w_h) R(\phi_h^{n+\theta})\, \mathrm{d}\Omega + \sum_K \int_K \frac{|R(\phi_h^{n+\theta})|}{|\nabla \phi_h^{n+\theta}|} (\nabla w_h \cdot \mathbf{H} \cdot \nabla \phi_h^{n+\theta})\, \mathrm{d}\Omega = l(w_h) \tag{7a}$$

$$R(\phi_h^{n+\theta}) := \frac{\phi_h^{n+\theta} - \phi_h^n}{\theta \Delta t} + \mathbf{u} \cdot \nabla \phi_h^{n+\theta} - \nabla \cdot (k \nabla \phi_h^{n+\theta}) + s \phi_h^{n+\theta} - f(\mathbf{x}) \tag{7b}$$

$$\phi_h^{n+1} = \frac{1}{\theta} \phi_h^{n+\theta} - \frac{(1-\theta)}{\theta} \phi_h^n \tag{7c}$$

where $0 < \theta \leqslant 1$ is the parameter of the generalized trapezoidal method. Clearly, if one is interested in the choice $\theta = 0$ then the temporal derivative term $(\phi_h^{n+\theta} - \phi_h^n)/(\theta \Delta t)$ that appears in Eqs. (7a) and (7b) should be replaced with $(\phi_h^{n+1} - \phi_h^n)/\Delta t$. In practice θ would not be taken below the value of 1/2 for unconditional temporal stability. In the transient numerical examples presented in Section 8.2 we have used the implicit midpoint rule which corresponds to the choice $\theta = 1/2$.

3. HRPG method in 1D

Naturally, the tensors **h** and **H** are reduced to scalar quantities in 1D. Taking the element size as ℓ, the counterparts of **h** and **H** in 1D are defined as

$$\mathbf{h} := \frac{\alpha}{2} \ell, \quad \mathbf{H} := \frac{\beta}{2} \ell \tag{8}$$

where α, β are stabilization parameters whose definition in 1D is summarized in Box 1. We now explain concisely the origins and the motivation behind this procedure to calculate the parameters α, β and refer to [48] for further details.

Box 1 Procedure to calculate the stabilization parameters α, β in 1D [48]. Adopted from [5, p. 316]. ℓ, Δt are the mesh element size and time-step, respectively. The time integration is done by the generalized trapezoidal method.

$$\gamma := \frac{u\ell}{2k}; \quad \omega := \frac{s\ell^2}{k}; \quad \sigma := \frac{s\ell}{u}$$

$$\lambda := \frac{1}{3\left(1 + \sqrt{|\sigma|}\right)}; \quad \boxed{\alpha := \lambda\, \mathrm{sgn}(u) \max\left\{\left[1 - \frac{1}{|\gamma|}\right], 0\right\}}$$

$$\overline{\delta} := \frac{1}{\theta \Delta t} \frac{\|\phi_h^{n+\theta} - \phi_h^n\|_\infty}{\|\phi_h^{n+\theta}\|_\infty}$$

$$\widetilde{u} := u - \frac{\alpha \ell s}{2} - \frac{\alpha \ell \overline{\delta}}{2}; \quad \widetilde{k} := k + \frac{\alpha \ell u}{2}; \quad \widetilde{s} := s + \overline{\delta}$$

$$\widetilde{\gamma} := \frac{\widetilde{u}\ell}{2\widetilde{k}}; \quad \widetilde{\omega} := \frac{\widetilde{s}\ell^2}{\widetilde{k}}; \quad \widetilde{\sigma} := \frac{\widetilde{s}\ell}{\widetilde{u}}$$

$$\boxed{\beta := \max\left\{\left[\frac{2}{3}\left(\frac{|\widetilde{\sigma}| + 3}{|\widetilde{\sigma}| + 2}\right) - \left(\frac{4}{\widetilde{\omega} + 4|\widetilde{\gamma}|}\right)\right], 0\right\}}$$

The HRPG method in 1D was designed using the divide and conquer strategy, i.e. the original CDR problem is further divided into smaller model problems where the different types of numerical artifacts that plague the original problem are singled-out and the expressions for the stabilization parameters are derived/updated to treat them effectively.

For the stationary CDR problem and by dropping the linear upwinding term (i.e. choosing $\alpha = 0$), the expression in 1D of the stabilization parameter β multiplying the shock-capturing term is found by relating it with the diffusion introduced by the

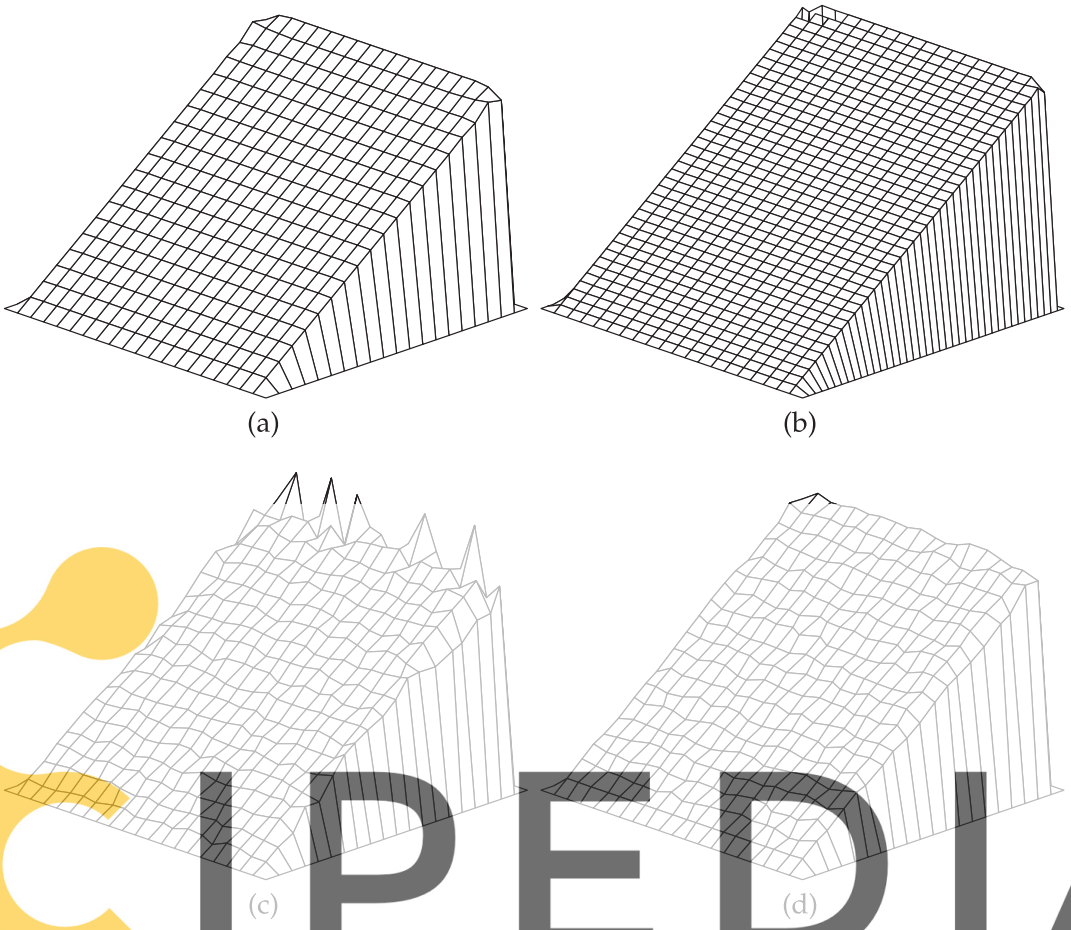

Fig. 8. Example 3, uniform advection with a constant source term. The solution of the HRPG method viewed at $(-45°, 20°)$ and using (a) a structured 20×20 mesh, (b) a structured 40×20 mesh, (c) an unstructured (Type I) 20×20 mesh, (d) an unstructured (Type II) 20×20 mesh.

discrete-upwinding operation [50] on the Galerkin terms. The proposed expression for β is (see [48, Section 5.4]):

$$\beta := \max\left\{\left[\frac{2}{3}\left(\frac{|\sigma|+3}{|\sigma|+2}\right)-\left(\frac{4}{\omega+4|\gamma|}\right)\right],0\right\} \tag{9}$$

where $\gamma := (u\ell/2k)$, $\omega := (s\ell^2/k)$ and $\sigma := (\omega/2\gamma) = (s\ell/u)$ are the element Peclect number, a velocity independent dimensionless number and the Damköler number respectively.

It was pointed out earlier in [46] that the transient term can be modeled as an instantaneous reaction term whose coefficient is inversely proportional to the employed time step. This observation is also the point of departure for methods designed to treat the small time step oscillations (essentially they are Gibbs phenomenon) [44,45]. Assuming that the discretization in time is done using the generalized trapezoidal method we define for each element a nonlinear pseudo-reaction coefficient $\overline{\delta}$ as follows

$$\overline{\delta} := \frac{1}{\theta\Delta t}\frac{\left\|\phi_h^{n+\theta}-\phi_h^n\right\|_\infty}{\left\|\phi_h^{n+\theta}\right\|_\infty} \tag{10}$$

Further, it was pointed out earlier in [22] that the linear upwinding term can be interpreted as to contribute additional convection (negative upwind direction) and diffusion (rank one tensor) effects. Using these ideas the effective convection, diffusion and reaction coefficients (for the transient problem and using the linear upwinding term) are calculated as follows

$$\widetilde{u} := u - \frac{\alpha\ell s}{2} - \frac{\alpha\ell\overline{\delta}}{2}; \quad \widetilde{k} := k + \frac{\alpha\ell u}{2}; \quad \widetilde{s} := s + \overline{\delta} \tag{11}$$

Thus, for the transient case and/or including the linear upwinding term, it is these effective coefficients that are used in the expression for β derived earlier. Thus,

$$\widetilde{\gamma} := \frac{\widetilde{u}\ell}{2\widetilde{k}}; \quad \widetilde{\omega} := \frac{\widetilde{s}\ell^2}{\widetilde{k}}; \quad \widetilde{\sigma} := \frac{\widetilde{s}\ell}{\widetilde{u}} \tag{12a}$$

$$\beta := \max\left\{\left[\frac{2}{3}\left(\frac{|\widetilde{\sigma}|+3}{|\widetilde{\sigma}|+2}\right)-\left(\frac{4}{\widetilde{\omega}+4|\widetilde{\gamma}|}\right)\right],0\right\} \tag{12b}$$

Remark 2. For the steady-state case, β depends only on the problem data, whereas for the transient case a nonlinear dependence exists due to Eq. (10). Such a nonlinear dependence which vanishes at steady state is necessary for the independence of the steady-state solution on the used time step. This additional nonlinearity which only affects β does not seem to increase the number of iterations required for convergence.

It remains to define the parameter α that controls the fraction of linear perturbation term in the HRPG method. For the 1D CDR problem the choice of the parameters: $\alpha = 0$ and β given by Eq. (12b) was sufficient to obtain accurate solutions for a wide range of problem data. Nevertheless for the transient problem the presence of the linear perturbation terms improved the convergence of the nonlinear iterations. Numerical experiments suggested $\alpha \in [0, 1/3]$ which means that the approximations/conjecture used in the design process does not hold for larger fractions of the linear perturbation term. The proposed expression for α is:

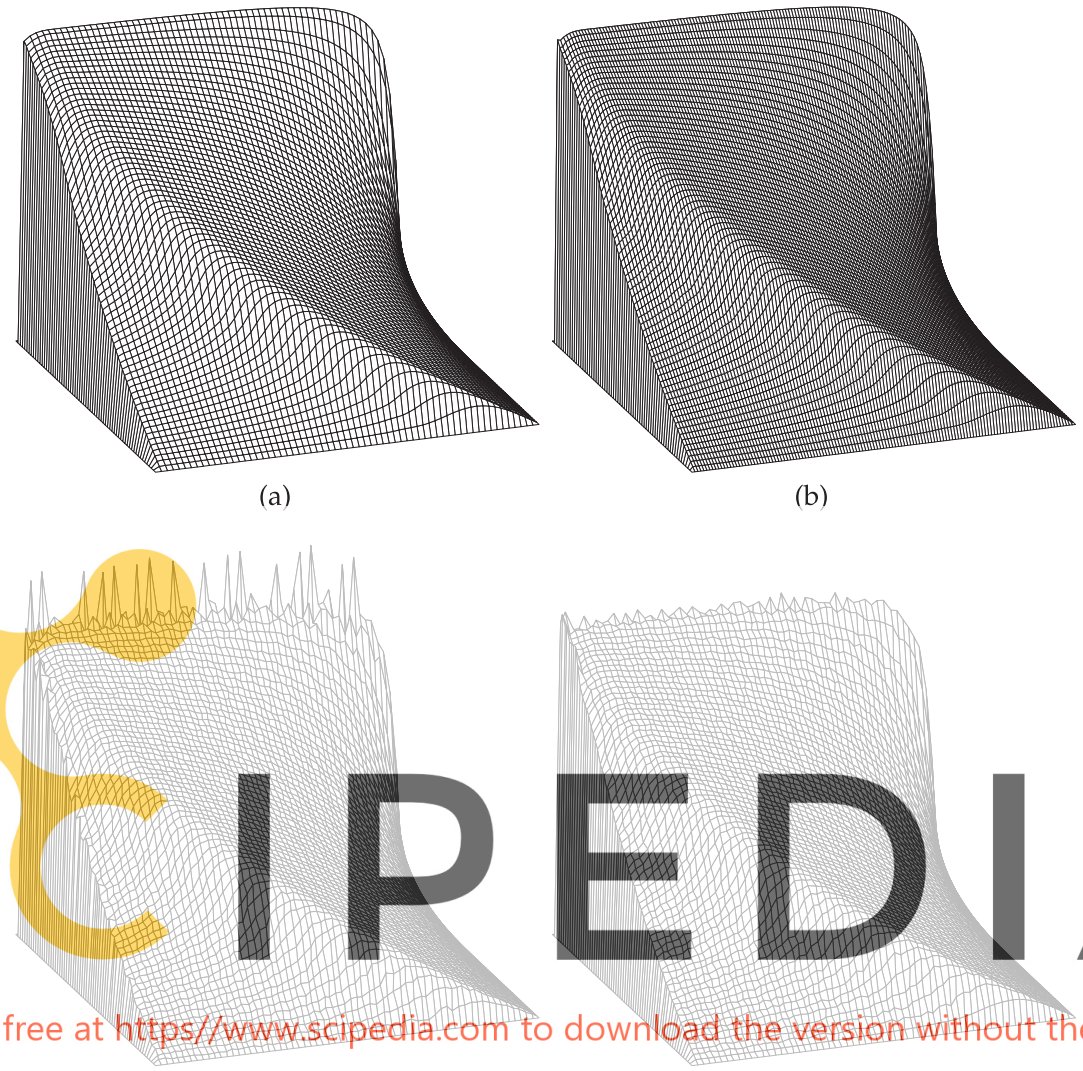

Fig. 9. Example 4, non-uniform advection with a constant source term. The solution of the HRPG method viewed at $(-200°, 20°)$ and using (a) a structured 64×64 mesh, (b) a structured 128×64 mesh, (c) an unstructured (Type I) 64×64 mesh, (d) an unstructured (Type II) 64×64 mesh.

$$\alpha := \lambda \ \mathrm{sgn}(u) \max\left\{\left[1 - \frac{1}{|\gamma|}\right], 0\right\}; \quad \lambda := \frac{1}{3(1+\sqrt{|\sigma|})} \tag{13}$$

Finally, we discuss the limit behavior of the stabilization parameters α and β in 1D. In the advective limit we have $\gamma \gg \omega$ i.e. $\sigma \to 0$ and in the reactive limit we have $\omega \gg \gamma$ i.e. $\sigma \to \infty$. In these respective limit cases we get from Eq. (13),

$$\lim_{\sigma\to 0} \alpha = \frac{\mathrm{sgn}(u)}{3} \max\left\{\left[1 - \frac{1}{|\gamma|}\right], 0\right\}; \quad \lim_{\sigma\to\infty} \alpha = 0 \tag{14}$$

In the diffusive limit we have both $\gamma, \omega \to 0$. In this case, as is required, from Eq. (13) we get $\alpha = 0$. In the presence of the linear upwinding term (i.e. $\alpha \neq 0$) it is more appropriate to discuss the effective limit behavior (convective, diffusive and reactive) of β. When the effective convection term dominates, we have $\widetilde{\gamma} \gg \widetilde{\omega}$ i.e. $\widetilde{\sigma} \to 0$. On the contrary, when the effective reaction term dominates we have $\widetilde{\omega} \gg \widetilde{\gamma}$ i.e. $\widetilde{\sigma} \to \infty$. In these respective limit cases we get from Eq. (12b),

$$\lim_{\widetilde{\sigma}\to 0} \beta = \max\left\{\left[1 - \frac{1}{|\widetilde{\gamma}|}\right], 0\right\}; \quad \lim_{\widetilde{\sigma}\to\infty} \beta = \max\left\{\left[\frac{2}{3} - \frac{4}{\widetilde{\omega}}\right], 0\right\} \tag{15}$$

When the effective diffusion term is dominant, we have $\widetilde{\gamma},\ \widetilde{\omega} \to 0$. In this case, as is required, from Eq. (12b) we get $\beta = 0$. Recall that the small time step limit falls within the case of the dominant effective reaction term. Thus, even for a pure diffusion problem, $\beta \to 2/3$ (as is required for the L^2 projection problem [48]), should the small time step limit be reached. The motivation to include this value for β in the small time step limit is based on the observation that the numerical artifacts found in this case are similar to the Gibbs phenomenon observed in L^2 projections. It was shown in [48], that these respective limit behaviors for β are required to attain high-resolution results.

4. Gibbs phenomenon across characteristic layers

The characteristic internal/boundary layers are usually found only in higher dimensions and hence have no instances in 1D [1]. In other words we do not have a straight-forward quantification of the characteristic layers in 1D. For this reason a direct extension of the definition of the stabilization parameters α, β derived for 1D will not be efficient to resolve these layers.

The numerical artifacts that are formed across the parabolic layers are usually manifested as the Gibbs phenomenon. Nevertheless there exists a subtle difference[1] between the numerical artifacts

[1] Related to the cause and size of these numerical artifacts.

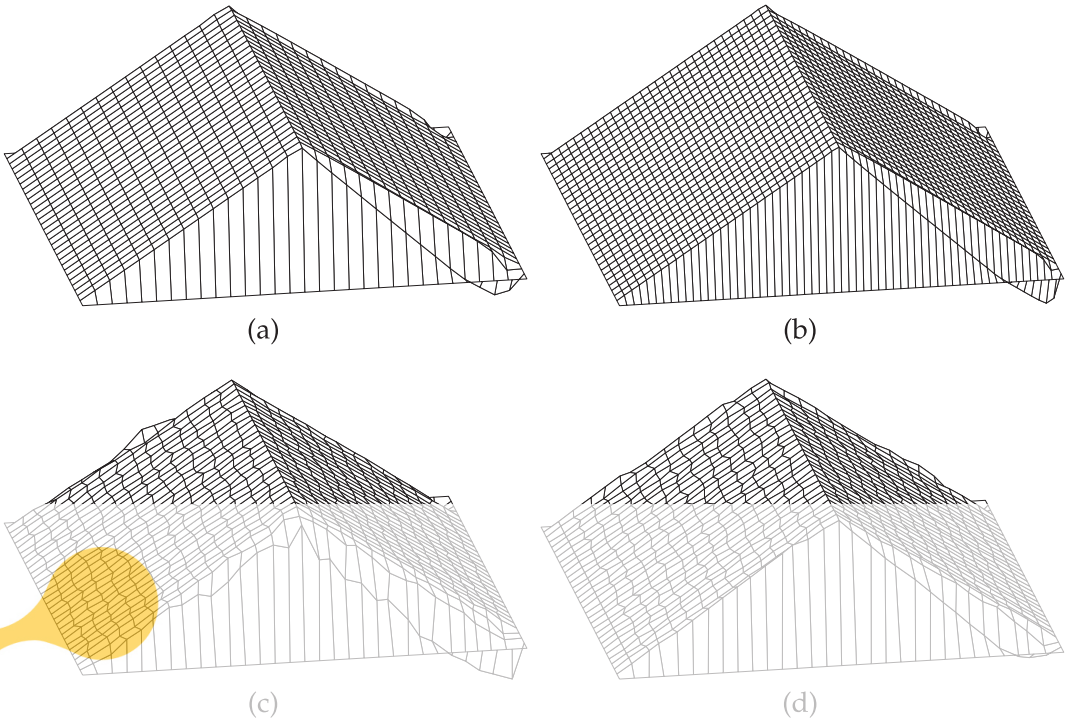

Fig. 10. Example 5, uniform advection with a discontinuous source term. The solution of the HRPG method viewed at $(-10°,20°)$ and using (a) a structured 30×30 mesh, (b) a structured 60×30 mesh, (c) an unstructured (Type I) 30×30 mesh, (d) an unstructured (Type II) 30×30 mesh.

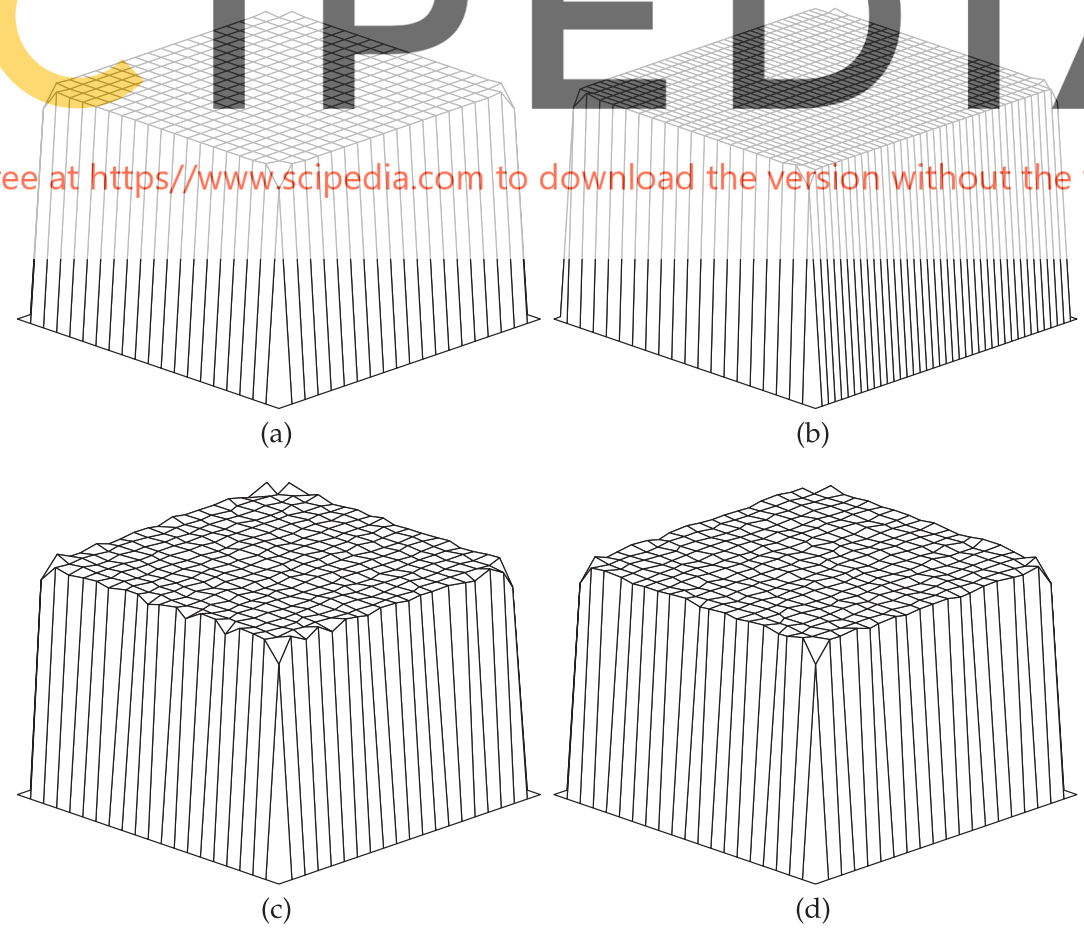

Fig. 11. Example 6, a reaction–diffusion problem The solution of the HRPG method viewed at $(-45°,20°)$ and using (a) a structured 20×20 mesh, (b) a structured 40×20 mesh, (c) an unstructured (Type I) 20×20 mesh, (d) an unstructured (Type II) 20×20 mesh.

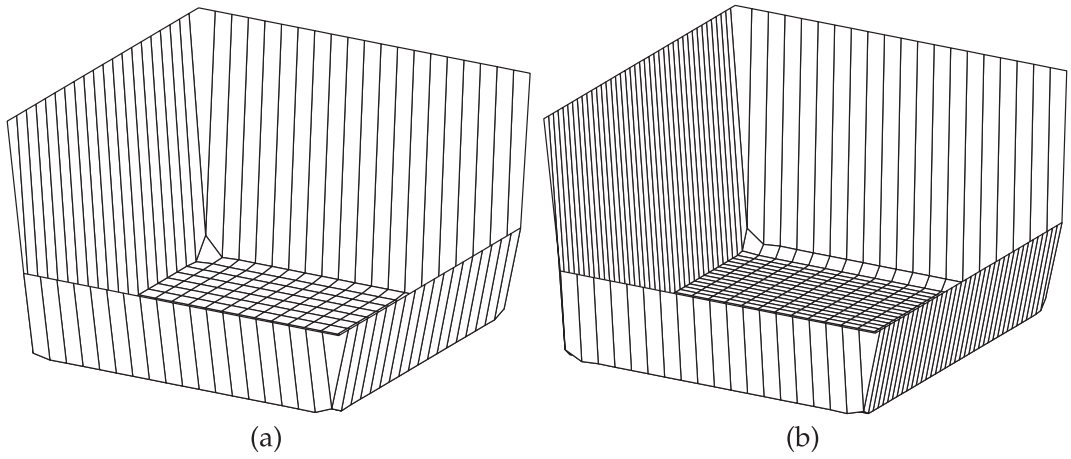

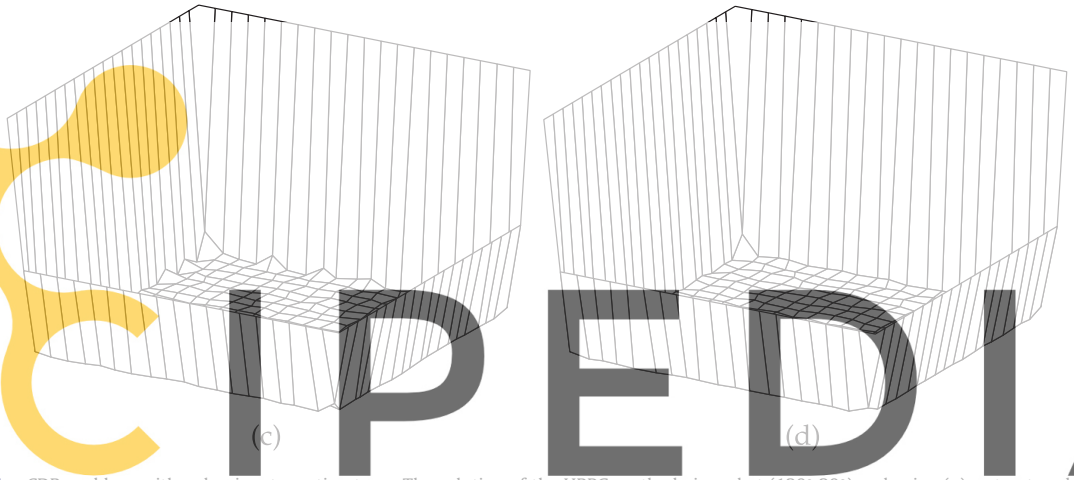

Fig. 12. Example 7, a CDR problem with a dominant reaction term. The solution of the HRPG method viewed at (120°,20°) and using (a) a structured 20 × 20 mesh, (b) a structured 40 × 20 mesh, (c) an unstructured (Type I) 20 × 20 mesh, (d) an unstructured (Type II) 20 × 20 mesh.

formed across the characteristic layers and those formed across the layers in the reaction-dominant cases. Consider a rectangular domain discretized by structured bilinear block finite elements. Let **A** represent the matrix of the stencil coefficients of a generic compact stencil corresponding to any interior node (i,j) of the considered structured mesh. For instance, if the standard mass matrix obtained in the Galerkin FEM be assembled for a structured rectangular mesh then we may express the corresponding stencil as follows:

$$\mathbf{A}^m := \frac{\ell_2}{6}\{1,4,1\}^{\mathrm{T}}\{1,4,1\}\frac{\ell_1}{6} = \frac{\ell_1\ell_2}{36}\begin{bmatrix}1 & 4 & 1\\ 4 & 16 & 4\\ 1 & 4 & 1\end{bmatrix} \tag{16}$$

where the superscript 'T' in the above equation denotes the transpose operator. The matrix $\mathbf{A}^m$ yields a stencil as shown below.

$$\mathbf{A}^m \mapsto \frac{\ell_1\ell_2}{36}\begin{Bmatrix}\Phi^{i-1,j+1} + 4\Phi^{ij+1} + \Phi^{i+1,j+1} +\\ 4\Phi^{i-1,j} + 16\Phi^{ij} + 4\Phi^{i+1,j} +\\ \Phi^{i-1,j-1} + 4\Phi^{ij-1} + \Phi^{i+1,j-1}\end{Bmatrix} \tag{17}$$

The stencil coefficient matrix associated with the convective term in the Galerkin FEM can be expressed as follows:

$$\mathbf{A}^c := \frac{\ell_2}{6}\{1,4,1\}^{\mathrm{T}}\{-1,0,1\}\frac{u_1}{2} + \frac{u_2}{2}\{1,0,-1\}^{\mathrm{T}}\{1,4,1\}\frac{\ell_1}{6} \tag{18}$$

Note that one may arrive at the terms in Eqs. (16) and (18) via a 1D mass type averaging of their respective counterparts in 1D, i.e. replacing $\{1,4,1\}(\ell_1/6)$ with $(\ell_2/6)\ \{1,4,1\}^{\mathrm{T}}\ \{1,4,1\}(\ell_1/6)$ and $\{-1,0,1\}(u_1/2)$ with $(\ell_2/6)\{1,4,1\}^{\mathrm{T}}\{-1,0,1\}(u_1/2)$, etc. Although this 1D mass type averaging leads to a higher-order approximation for smooth solution profiles, it unfortunately leads to the Gibbs phenomenon across layers. Unlike in the reaction-dominant case where it is the numerical solution that undergoes the 1D mass type averaging, in the convection-dominant case it is the derivatives of the numerical solution that undergoes the same. Thus, the Gibbs phenomenon across the characteristic layers in the later case is proportional to the variation in the derivatives of the solution across the characteristic layers. Despite this subtle difference in the Gibbs phenomenon associated with the characteristic layers in the convection-dominated case, we choose to treat them by the same strategy that we use to treat the numerical artifacts about the parabolic layers in the reaction-dominant case. The pros and cons of employing this strategy will be discussed later in Section 8.3.

5. Quantifying characteristic layers

In this section we design a nondimensional element number that quantifies the characteristic internal/boundary layers. By quantification we mean that its should serve a similar purpose as the element Peclet number γ for the exponential layers in convection dominant cases and the dimensionless number $\omega := 2\gamma\sigma$ for the parabolic layers in the reaction dominant cases.

Consider the following singularly perturbed $(k \ll u)$ convection–diffusion problem in 2D:

Table 2
A comparison of the maximum and minimum values of the HRPG and the exact (shown in square brackets) solutions in the examples presented in Section 8.1. The number of nonlinear iterations required for convergence using a tolerance of 1e−2, 1e−3 and 1e−4 are also shown side by side.

Example	max(ϕ_h)[max(ϕ)]	min(ϕ_h)[min(ϕ)]	Iterations		
			1e−2	1e−3	1e−4
1, Fig. 6(a)	1.0029 [1.0]	−3.4857e−005 [0.0]	3	6	10
1, Fig. 6(b)	1.005 [1.0]	−3.5839e−007 [0.0]	3	6	9
1, Fig. 6(c)	1.0499 [1.0]	−1.9485e−006 [0.0]	3	6	9
1, Fig. 6(d)	1.0166 [1.0]	−2.8334e−005 [0.0]	3	5	9
2, Fig. 7(a)	1.0034 [1.0]	−0.004592 [0.0]	3	7	13
2, Fig. 7(b)	1.0041 [1.0]	−0.0024418 [0.0]	3	7	13
2, Fig. 7(c)	1.0303 [1.0]	−0.0060189 [0.0]	3	7	11
2, Fig. 7(d)	1.0524 [1.0]	−0.012783 [0.0]	3	8	14
3, Fig. 8(a)	0.95031 [0.95]	0.0 [0.0]	3	5	9
3, Fig. 8(b)	0.97665 [0.975]	0.0 [0.0]	3	5	8
3, Fig. 8(c)	1.1076 [<1.0]	0.0[0.0]	3	7	14
3, Fig. 8(d)	0.96857 [0.95]	0.0 [0.0]	3	6	16
4, Fig. 9(a)	1.5517 [<1.5708]	0.0 [0.0]	1	5	>20
4, Fig. 9(b)	1.5529 [<1.5708]	0.0 [0.0]	1	5	>20
4, Fig. 9(c)	1.8138 [<1.5708]	0.0 [0.0]	5	9	>20
4, Fig. 9(d)	1.6191 [<1.5708]	0.0 [0.0]	4	8	>20
5, Fig. 10(a)	0.5 [0.5]	−0.068137 [0.0]	3	7	13
5, Fig. 10(b)	0.50002 [0.5]	−0.10108 [0.0]	3	7	12
5, Fig. 10(c)	0.50182 [0.5]	−0.12577 [0.0]	3	7	18
5, Fig. 10(d)	0.50689 [0.5]	−0.057931 [0.0]	3	7	13
6, Fig. 11(a)	1.0053 [1.0]	0.0 [0.0]	3	7	10
6, Fig. 11(b)	1.0096 [1.0]	0.0 [0.0]	3	6	9
6, Fig. 11(c)	1.03 [1.0]	0.0 [0.0]	3	7	10
6, Fig. 11(d)	1.0148 [1.0]	0.0 [0.0]	3	7	10
7, Fig. 12(a)	1.0 [1.0]	−0.0041651 [0.0]	4	7	10
7, Fig. 12(b)	1.0 [1.0]	−0.0030349 [0.0]	4	6	9
7, Fig. 12(c)	1.0 [1.0]	−0.02101 [0.0]	4	7	10
7, Fig. 12(d)	1.0 [1.0]	−0.0080537 [0.0]	4	7	10

$$u\frac{\partial\phi}{\partial x} - k\left(\frac{\partial^2\phi}{\partial x^2} + \frac{\partial^2\phi}{\partial y^2}\right) = 0 \quad \text{in } \Omega \tag{19a}$$

$$\phi = \phi^p \quad \text{on } \Gamma \tag{19b}$$

where Ω is a rectangular domain *ABCD* as shown in Fig. 1(a), Γ is the domain boundary and ϕ^p is the prescribed value of ϕ on Γ. The origin of the 2D axes is taken as the midpoint of *AD*. Consider $\phi^p = 0$ everywhere except on *AD* where it is defined as follows:

$$\phi^p(0,y) = f(y) := \mathrm{H}(y+a) - \mathrm{H}(y-a), \quad a > 0 \tag{20a}$$

$$\mathrm{H}(y) := \frac{1+\mathrm{sgn}(y)}{2} = \begin{cases} 0 & y < 0 \\ 0.5 & y = 0 \\ 1 & y > 0 \end{cases} \tag{20b}$$

The function $f(y)$ is discontinuous at $y = \pm a$ and its shape can be described as a rectangular pulse. A well known virtue of the solution $\phi(x,y)$ is that these discontinuities are immediately smoothed out in the interior of the domain, thus leading to parabolic layers along the characteristic lines of the problem [1]. In accordance with singular perturbation theory and by the method of matched asymptotic expansions [51], the leading term describing the characteristic layer is given by,

$$\phi(x,y) \approx \frac{1}{2}\left[\mathrm{erf}\left(\sqrt{\frac{u}{4kx}}(y+a)\right) - \mathrm{erf}\left(\sqrt{\frac{u}{4kx}}(y-a)\right)\right] \tag{21}$$

where 'erf' represents the *error function* and is defined as follows:

$$\mathrm{erf}(x) := \frac{2}{\sqrt{\pi}}\int_0^x e^{-z^2}\,\mathrm{d}z \tag{22}$$

The approximation given in Eq. (21) is uniformly valid to $O(1)$ in a region away from the exponential layers formed near the boundary *BC* [51]. Fig. 1(b) illustrates the solution given by Eq. (21) about a cross-section *SS′* (cf. Fig. 1(b)) located at a distance x from the boundary *AD*.

Consider now the heat equation posed on an infinite domain:

$$\frac{\partial\phi}{\partial t} - k\frac{\partial^2\phi}{\partial y^2} = 0, \quad \text{in } \Omega := \{(y,t)|y \in (-\infty,\infty), t \in [0,\infty)\} \tag{23a}$$

$$\phi(y, t=0) = f(y) \quad f(y) := [\mathrm{H}(y+a) - \mathrm{H}(y-a)], \quad a > 0 \tag{23b}$$

Note that we have initialized the solution with a function $f(y)$ that was used earlier in Eq. (20a) to prescribe the Dirichlet boundary condition. The exact solution for the problem (23) can be expressed as follows:

$$\phi(y,t) = \frac{1}{2}\left[\mathrm{erf}\left(\frac{y+a}{\sqrt{4kt}}\right) - \mathrm{erf}\left(\frac{y-a}{\sqrt{4kt}}\right)\right] \tag{24}$$

Clearly, replacing t with (x/u) in Eq. (24) we recover the leading term describing the characteristic layers given by Eq. (21). Note that (x/u) is the time required to travel a distance x along the characteristic lines. This resemblance is due to the fact that in regions far-away from the domain boundaries the convective and diffusive effects do not interact, i.e. convection just carries the diffusing solution along the characteristic lines [52].

Next, we try to relate the solution of the heat equation with the solution of the diffusion–reaction problem. The statement of the diffusion–reaction problem posed on an infinite domain is:

$$-k\frac{d^2\phi}{dy^2} + s\phi = sf(y) \quad \text{in } \Omega := \{y|y \in (-\infty,\infty)\} \tag{25a}$$

$$\phi(y) = 0 \quad \text{at } y = \pm\infty \tag{25b}$$

The exact solution for the above problem can be expressed as follows:

$$\phi(y) = \frac{\mathrm{sgn}(y+a)}{2}[1 - e^{-\xi|y+a|}] - \frac{\mathrm{sgn}(y-a)}{2}[1 - e^{-\xi|y-a|}] \tag{26}$$

where, $\xi := \sqrt{s/k}$. Fig. 2(a) and (b) illustrate the solution of the heat equation given by Eq. (24) and the solution of the diffusion–reaction problem given by Eq. (26) respectively. Clearly these two solutions

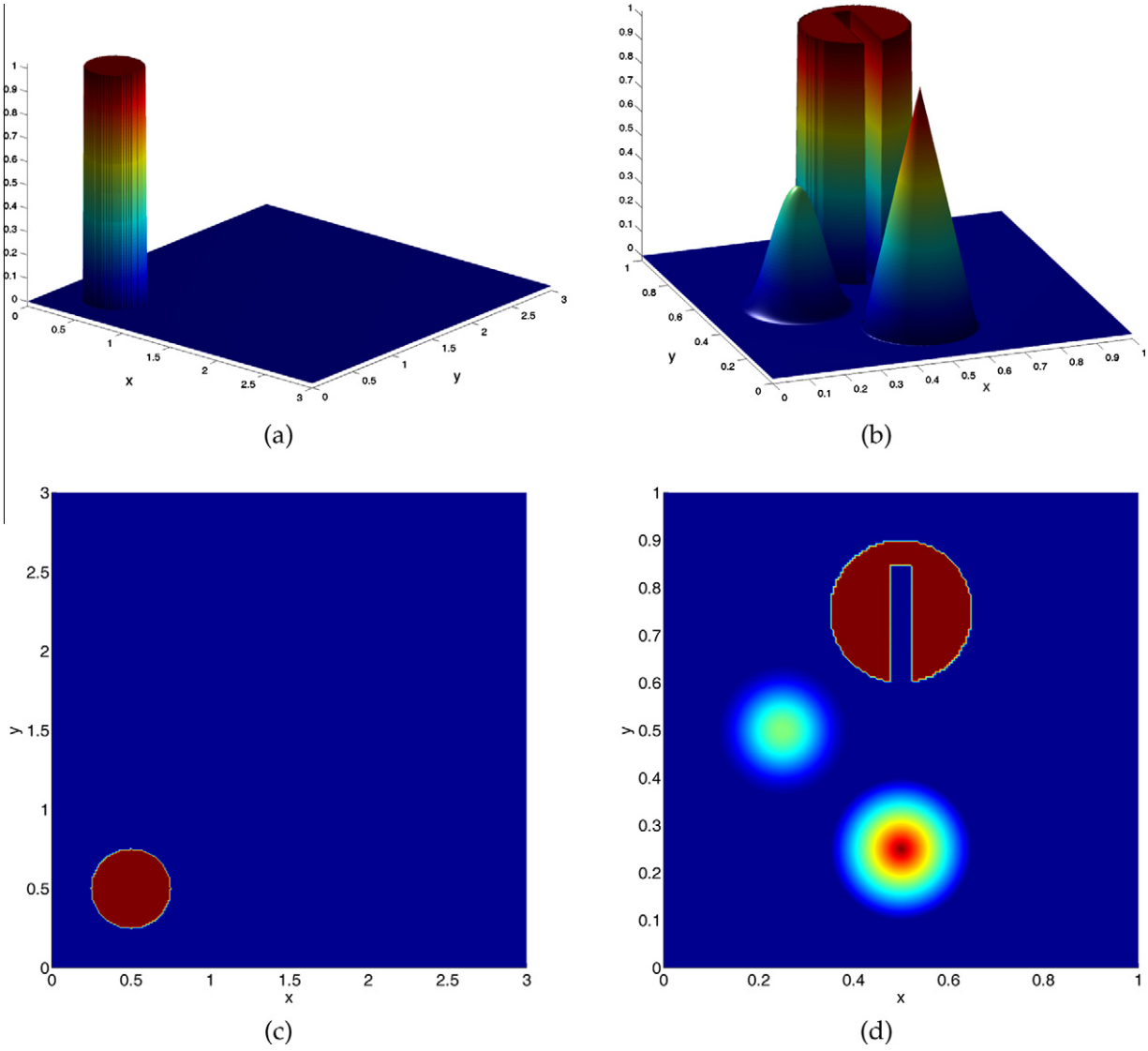

Fig. 13. Initial data for the transient 2D advection examples. (a) Example 8, elevation plot viewed at (40°,20°), (b) Example 9, elevation plot viewed at (−20°,20°), (c) Example 8, contour plot, (d) Example 9, contour plot.

have distinct profiles. Nevertheless, they share a common trait of possessing parabolic layers, i.e. the first-order derivatives in the direction perpendicular to the layers have magnitude $O\left(1/\sqrt{k}\right)$. We refer to [1] for further details about parabolic and exponential layers.

Now we pose the following design problem: *Relate s and t such that the parabolic layers in the solution of the heat equation i.e.* Eq. (24) *and the solution of the diffusion–reaction problem i.e.* Eq. (26) *have the same width.*

In the following developments the width of the layer is taken as the distance within which the value of ϕ varies from 1% to 99% of $[\max(f(y)) - \min(f(y))]$. We choose $f(y) = H(y)$ to simplify the algebra. For this choice of $f(y)$ the solution of the heat equation and the diffusion–reaction problem can be expressed as in Eqs. (27) and (28) respectively.

$$\phi(y,t) = \frac{1}{2}\left[1 + \operatorname{erf}\left(\frac{y}{\sqrt{4kt}}\right)\right] \tag{27}$$

$$\phi(y) = \frac{1}{2}[1 + \operatorname{sgn}(y)(1 + e^{\xi|y|})] \tag{28}$$

Let $y = -y^*$ be the distance at which the solutions given by Eqs. (27) and (28) have a value equal to 1% of $[max(H(y)) - min(H(y))]$, i.e. 0.01. Due to the inherent symmetry of the problem, these solutions at $y = y^*$ will attain a value equal to 99% of $[max(H(y)) - min(H(y))]$, i.e. 0.99. Thus we have,

$$\frac{1}{2}\left[1 + \operatorname{erf}\left(\frac{-y^*}{\sqrt{4kt}}\right)\right] = \frac{1}{100} = \frac{e^{-\xi y^*}}{2} \tag{29}$$

Solving Eq. (29) we get the following equation relating s and t,

$$st = \frac{1}{4}\left[\frac{\ln(50)}{\operatorname{erf}^{-1}(49/50)}\right]^2 \approx \sqrt{2} \Rightarrow \boxed{s \approx \frac{\sqrt{2}}{t}} \tag{30}$$

The above relation between s and t guarantees that the parabolic layers that appear in the solutions of the heat equation and the diffusion–production problem will have the same width. In Fig. 3 using Eq. (30) these solutions having the same layer width are compared.

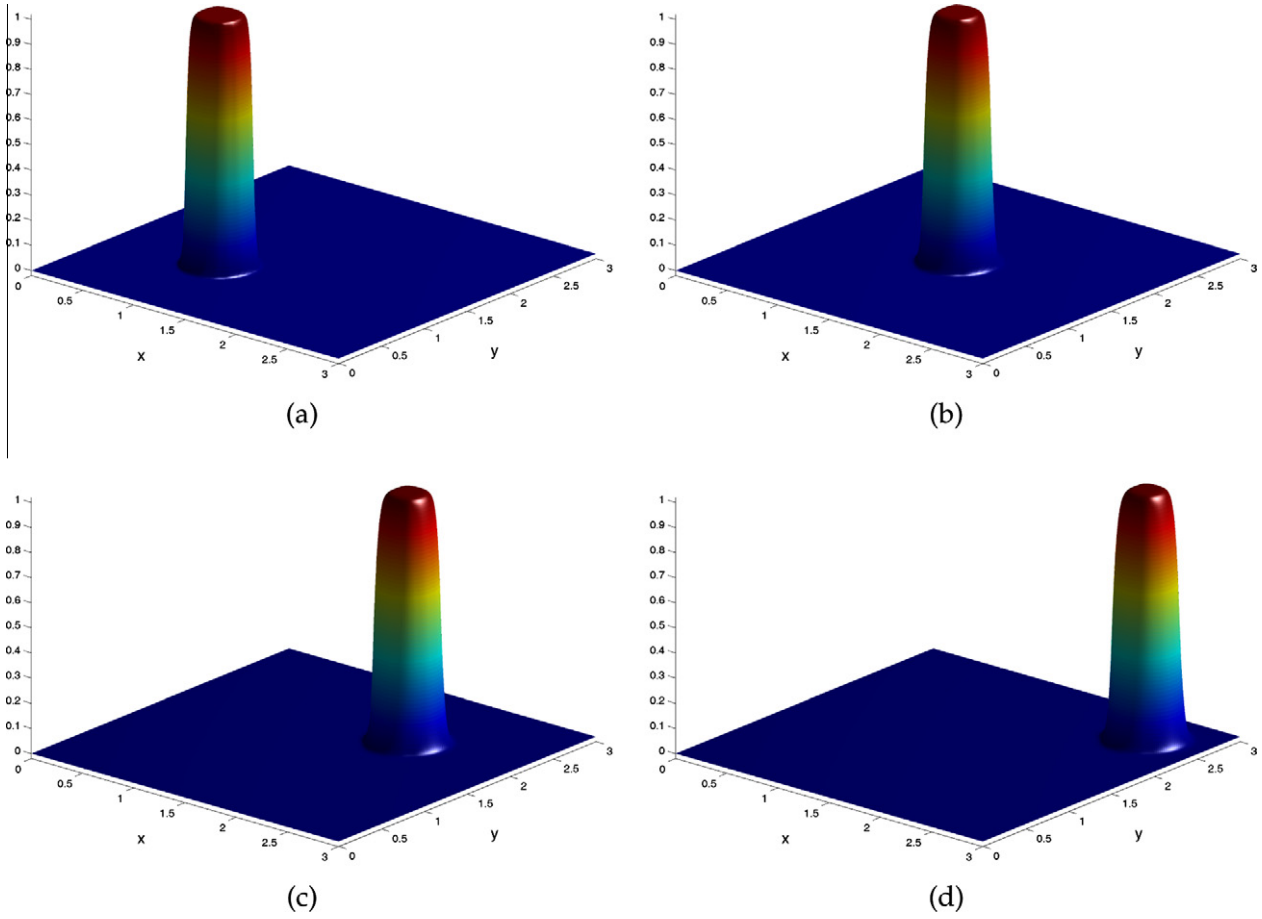

Fig. 14. Example 8, transient pure convection skew to the mesh. The solution of the HRPG method viewed at (40°, 20°) and at time (a) $t = 1$ s, (b) $t = 2$ s, (c) $t = 3$ s, (d) $t = 4$ s.

Remark 3. Using Eq. (30) an alternate *linear* model for the pseudo-reaction coefficient could be $\overline{\delta} := \sqrt{2}/t^{n+\theta} = \sqrt{2}/(n+1-\theta)\Delta t$. Recall that the earlier expression for $\overline{\delta}$ given in Eq. (10) is *nonlinear*. The motivation for this nonlinear dependence is to guarantee the independence of the steady-state solution on the used time step. Using $\overline{\delta} := \sqrt{2}/(n+1-\theta)\Delta t$ will make the parameter β independent of the solution even for the transient case. Further, the steady-state case has to be understood as $n \gg 1$ i.e. $t^{n+\theta} \to \infty$ and here, as required, $\overline{\delta} \to 0$. The pros and cons of using this $\overline{\delta}$ instead of the one given earlier in Eq. (10) will be explored in future works.

We now address the initial objective of quantifying the characteristic layers found in the singularly perturbed convection–diffusion problem (19). Consider a fictitious reaction coefficient s_c and an associated dimensionless element number ω_c defined as below.

$$s_c := \frac{\sqrt{2}u}{x}, \quad \omega_c = \frac{s_c \ell^2}{k} \tag{31}$$

where ℓ is an appropriate element length measure. We have used the substitution $t = (x/u)$ in Eq. (30) to arrive at the expression for s_c in Eq. (31). Recall that we have used earlier the same substitution in the solution of the heat equation to recover the leading term describing the characteristic layers in the solution of the convection–diffusion problem. We may use this fictitious reaction coefficient s_c to relate the characteristic layers of the convection–diffusion problem to similar[2] parabolic layers of the 1D diffusion–production problem. In this sense, the nondimensional element number ω_c quantifies the characteristic layers and could be used in the design of stabilization parameters to control the numerical artifacts about these layers.

Note that the value of s_c is a function of x, i.e. s_c is inversely proportional to the distance from the source of the discontinuity along the characteristic lines. In fact this is how the characteristic layers in the solution of the convection–diffusion problem behave, i.e. their width widens as we move away from the source of the discontinuity along the characteristic lines. However from the design point-of-view, a variable definition of s_c and hence of ω_c is inconvenient. This is due to the fact that the characteristic lines could be arbitrary curves governed by the velocity field and hence finding the distance x along these lines need not be straight-forward. Hence we redefine s_c and ω_c using an appropriate element characteristic length ℓ_c which effectively models the sharpest characteristic layer close to the inflow boundary

$$s_c := \frac{\sqrt{2}u}{\ell_c}, \quad \omega_c = \frac{s_c \ell^2}{k} \tag{32}$$

6. Objective characteristic tensors

In this section we present the objective characteristic tensors **h** and **H** used in the extension of the HRPG method to higher dimensions. In the developments to follow, only the lowest order block finite elements are considered. Here *objectivity* is to be understood as the independence of the method on the description of the reference frame and admissible node numbering permutations of the mesh.

[2] In the sense of matched layer widths.

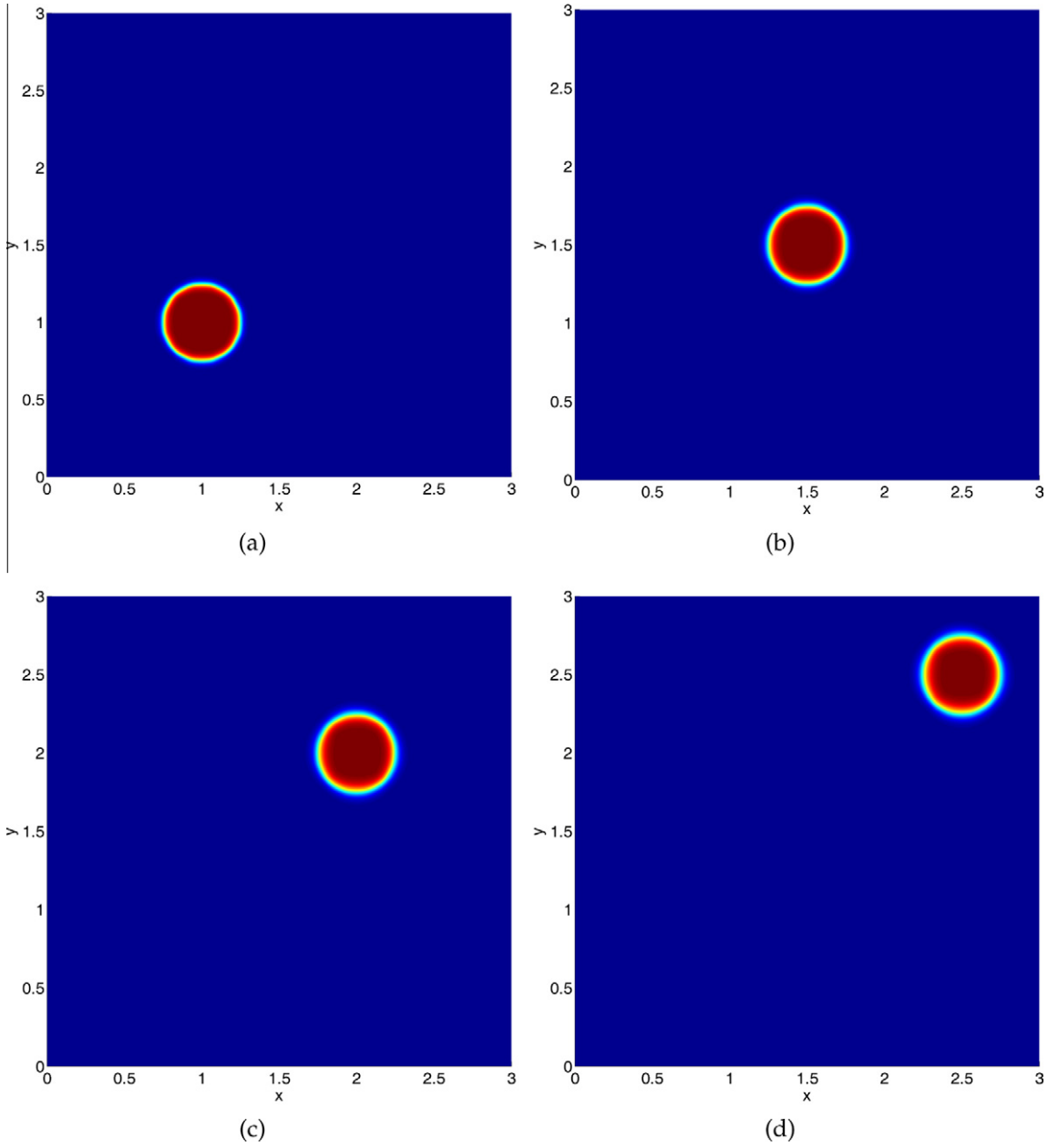

Fig. 15. Example 8, transient pure convection skew to the mesh. The contour plots of the solution of the HRPG method at time (a) $t = 1$ s, (b) $t = 2$ s, (c) $t = 3$ s, (d) $t = 4$ s.

Consider the following definition for the element length vectors $\mathbf{l}^i$:

$$\boxed{\mathbf{l}^i := 2\mathbf{J}\cdot\widetilde{\mathbf{e}}^i;} \quad \mathrm{J}_{ij} := \frac{\partial x_i}{\partial \widetilde{x}_j}; \quad \widetilde{\mathrm{e}}^i_j := \delta^i_j \tag{33}$$

where $\mathbf{J}$ represents the Jacobian matrix of bijective mappings from the local to global coordinate systems, x_i and $\widetilde{x}_i$ represent the global and local coordinates respectively, $\widetilde{\mathbf{e}}^i$ are fixed vectors along the axes of the local frame and δ^i_j is the Kronecker delta. Fig. 4 illustrates the element length vectors $\mathbf{l}^i$ obtained at any arbitrary point $P(\widetilde{x}_1, \widetilde{x}_2)$ within a 2D bilinear block finite element. The expression for the vectors $\mathbf{l}^i$ in 2D and at this point P can be simplified to the following:

$$\mathbf{l}^1 = \frac{1-\widetilde{x}_2}{2}\mathbf{E}^{12} + \frac{1+\widetilde{x}_2}{2}\mathbf{E}^{43}; \quad \mathbf{l}^2 = \frac{1-\widetilde{x}_1}{2}\mathbf{E}^{14} + \frac{1+\widetilde{x}_1}{2}\mathbf{E}^{23} \tag{34}$$

where $\mathbf{E}^{ab}$ is the edge vector pointing from node a to node b.

Let α^i, β^i be stabilization parameters calculated along the element length vectors $\mathbf{l}^i$ and with the following properties: (a) $(\mathbf{u}\cdot\mathbf{l}^i)\alpha^i \geqslant 0\ \forall i$, (b) $\beta^i \geqslant 0\ \forall i$ and (c) only scalars and free vectors[3] are used in their respective definitions. The definition of these parameters is delayed until Section 7. The characteristic tensors $\mathbf{h}$ and $\mathbf{H}$ are calculated as: $\mathbf{h} := 0.5\alpha^i\mathbf{l}^i$, $\mathbf{H} := 0.5(\beta^i/|\mathbf{l}^i|)[\mathbf{l}^i \otimes \mathbf{l}^i]$. Thus in 2D the characteristic tensors could be expressed as follows:

$$\mathbf{h} := \alpha^1\mathbf{l}^1 + \alpha^2\mathbf{l}^2; \quad \mathbf{H} := \frac{\beta^1}{|\mathbf{l}^1|}[\mathbf{l}^1 \otimes \mathbf{l}^1] + \frac{\beta^2}{|\mathbf{l}^2|}[\mathbf{l}^2 \otimes \mathbf{l}^2] \tag{35}$$

Using $\mathbf{h}$, $\mathbf{H}$ as defined above we calculate the perturbation p_h associated with the HRPG method as described earlier in Eq. (6). The definition of $\mathbf{h}$ and $\mathbf{H}$ given by Eq. (35) guarantees the

[3] If one is interested only in the magnitude and direction of the vector and does not think of it as situated at any particular location, then it is called a free vector.

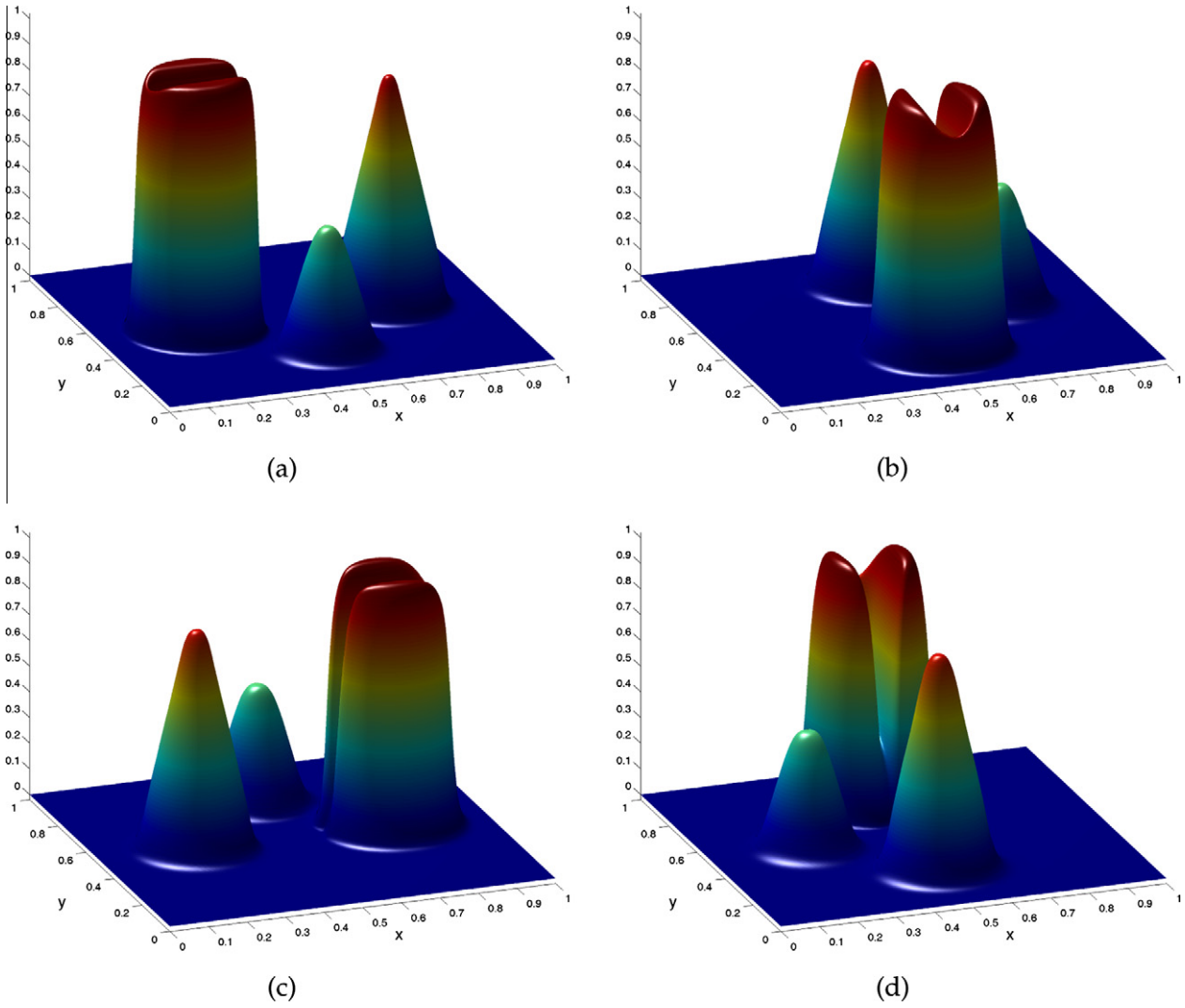

Fig. 16. Example 9, rotation of solid bodies. The solution of the HRPG method viewed at $(-20°, 20°)$ and at time (a) $t = (\pi/2)$ s i.e. after a quarter-revolution, (b) $t = \pi$ s i.e. after a half-revolution, (c) $t = (3\pi/2)$ s, i.e. after three quarters of a revolution (d) $t = 2\pi$ s i.e. after a full-revolution.

objectivity of the HRPG method. Reference frame independence can be verified by the fact that the tensors **h** and **H** obey the same tensor transformation rules as any other free tensor associated with the problem, e.g. the velocity vector **u**. Admissible node numbering permutations only swap one element length vector with the other (possibly with a change of sign) as shown in Fig. 4(b). Due to the properties of α^i, β^i and by their definition, the characteristic tensors **h** and **H** are invariant with respect to these swaps in $\mathbf{l}^i$.

Remark 4. Figures similar to Fig. 4(a) were presented earlier in [2] (cf. Fig. 3.2, p. 55), [3] (cf. Fig. 3.4, p. 215) and [53] (cf. Fig. 2, p. 2205). Therein the element length vectors $\mathbf{l}^i$ evaluated at the centroid of the element were used to define a *scalar* element size measure. The distinction here is to use these $\mathbf{l}^i$ to arrive at *objective characteristic tensors* **h** and **H** that treat effectively the anisotropy of the finite element.

Remark 5. Consider a rectangular domain partitioned by structured bilinear block finite elements with dimensions ℓ_1, ℓ_2, respectively. It was observed for the FIC method that the exponential layers are better resolved choosing $\mathbf{h}^{\text{fic}} = \{\alpha^1\ell_1, \alpha^2\ell_2\}$ instead of $\mathbf{h}^{\text{fic}} = \tau\mathbf{u}$. Making the latter choice we recover the SUPG method and here one often finds partially resolved global oscillations when the velocity is skewed to the mesh or using high aspect ratio FEs. Following this line, a more elaborate approach was presented in [54] within the framework of subgrid scale methods, to define a scalar expression for the stabilization parameter τ that render the method robust with respect to the mesh distortion. In the FIC method this robustness is achieved by the inclusion of additional, albeit simple (a straight-forward extension of their 1D counterparts), parameters (here α^1 and α^2). However special care has to be taken such that the characteristic length $\mathbf{h}^{\text{fic}}$ be objective. This is the motivation behind the way the characteristic tensors **h** and **H** are designed in the HRPG method.

7. Stabilization parameters

Except for the modification to include the new dimensionless number introduced in Section 5 that quantifies the characteristic layers, the definition of the stabilization parameters α^i, β^i calculated along the element length vectors $\mathbf{l}^i$ are a direct extension of their counterparts in 1D summarized in Box 1. Following this line, in multi dimensions and along $\mathbf{l}^i$ we define the following nondimensional element numbers:

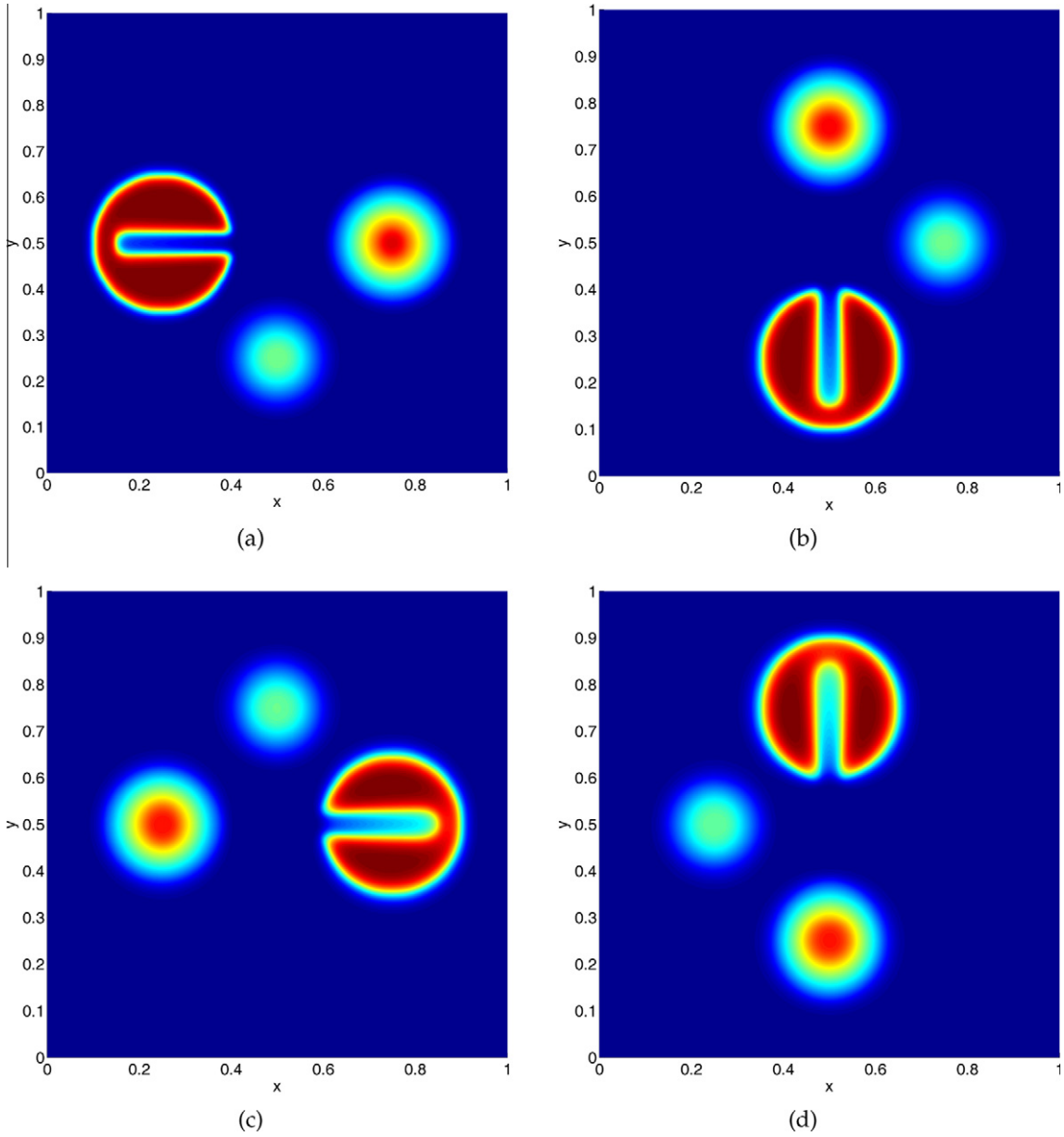

Fig. 17. Example 9, rotation of solid bodies. The contour plots of the solution of the HRPG method at time (a) $t = (\pi/2)$ s i.e. after a quarter-revolution, (b) $t = \pi$ s i.e. after a half-revolution, (c) $t = (3\pi/2)$ s, i.e. after three quarters of a revolution, (d) $t = 2\pi$ s i.e. after a full-revolution.

$$\gamma^i := \frac{\mathbf{u}\cdot\mathbf{l}^i}{2k}; \quad \omega^i := \frac{s|\mathbf{l}^i|^2}{k}; \quad \sigma^i := \frac{s|\mathbf{l}^i|^2}{\mathbf{u}\cdot\mathbf{l}^i} \tag{36}$$

Following Eq. (32), the fictitious reaction coefficient $\widehat{s}^i$ and the associated dimensionless number $\widehat{\omega}^i$ along $\mathbf{l}^i$ are calculated as follows.

$$\widehat{s}^i := \max_{j\neq i} \sqrt{2}\frac{|\mathbf{u}\cdot\mathbf{l}^j|}{|\mathbf{l}^j|^2}; \quad \widehat{\omega}^i := \frac{\widehat{s}^i|\mathbf{l}^i|^2}{k} \tag{37}$$

Following Eq. (13) the stabilization parameters α^i along $\mathbf{l}^i$ are calculated as follows.

$$\boxed{\alpha^i := \lambda^i \ \mathrm{sgn}(\mathbf{u}\cdot\mathbf{l}^i)\max\left\{\left[1-\frac{1}{|\gamma^i|}\right],0\right\};} \quad \lambda^i := \frac{1}{3\left(1+\sqrt{|\sigma^i|}\right)} \tag{38}$$

Assuming that the discretization in time is done using the implicit trapezoidal rule and following Eq. (10) we calculate the nonlinear pseudo-reaction coefficient $\overline{\delta}$ as follows

$$\overline{\delta} := \frac{1}{\theta\Delta t}\frac{\|\widetilde{\phi}_h - \phi_h^n\|_\infty}{\|\widetilde{\phi}_h\|_\infty} \tag{39}$$

Following Eq. (11) we define the effective convection, diffusion and reaction coefficients along $\mathbf{l}^i$ as follows

$$\widetilde{u}^i := \frac{\mathbf{u}\cdot\mathbf{l}^i}{|\mathbf{l}^i|} - \frac{\alpha^i|\mathbf{l}^i|s}{2} - \frac{\alpha|\mathbf{l}^i|\overline{\delta}}{2}; \quad \widetilde{k}^i := k + \frac{\alpha^i\mathbf{u}\cdot\mathbf{l}^i}{2}; \quad \widetilde{s} := s + \overline{\delta} \tag{40}$$

Likewise following Eq. (12a), the effective element dimensionless numbers along $\mathbf{l}^i$ can be calculated as,

$$\widetilde{\gamma}^i := \frac{|\widetilde{u}^i||\mathbf{l}^i|}{2\widetilde{k}^i}; \quad \widetilde{\sigma}^i := \frac{\widetilde{s}|\mathbf{l}^i|}{|\widetilde{u}^i|}; \quad \widetilde{\omega}^i := \frac{\widetilde{s}|\mathbf{l}^i|^2}{\widetilde{k}^i} \tag{41}$$

Finally, following Eq. (12b) the stabilization parameters β^i along $\mathbf{l}^i$ are calculated using the dimensionless numbers $\widetilde{\gamma}^i$, $\widetilde{\sigma}^i$, $\widetilde{\omega}^i$ and $\widehat{\omega}^i$ as follows:

$$\boxed{\beta^i := \max\left\{\left[\frac{2}{3}\left(\frac{\widetilde{\sigma}^i+3}{\widetilde{\sigma}^i+2}\right)-\left(\frac{4}{\widetilde{\omega}^i+4\widetilde{\gamma}^i}\right)\right],\left[\frac{2}{3}-\frac{4}{\widehat{\omega}^i}\right],0\right\}} \tag{42}$$

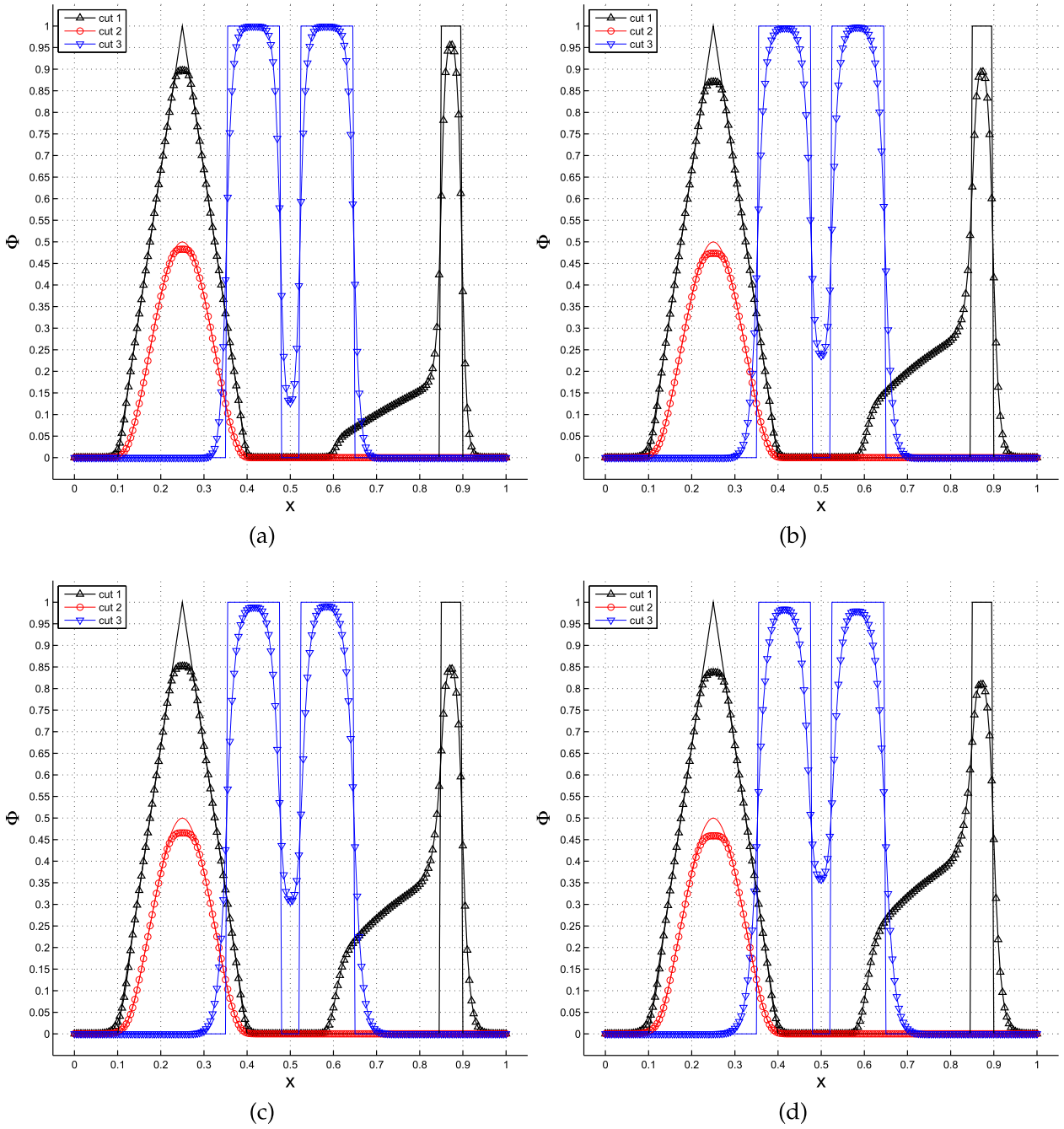

Fig. 18. Example 9, rotation of solid bodies. Three different cross sections (cut 1, cut 2 and cut 3) of the HRPG solution are shown at time (a) $t = (\pi/2)$ s i.e. after a quarter-revolution, (b) $t = \pi$ s i.e. after a half-revolution, (c) $t = (3\pi/2)$ s, i.e. after three quarters of a revolution, (d) $t = 2\pi$ s i.e. after a full-revolution. The solid lines without markers are the true solution.

The inclusion of the term $(2/3) - (4/\widehat{\omega}^i)$ in the definition of β^i is the only modification from a straight-forward extension to multi dimensions of the definition of its counterpart in 1D. This expression follows from the reaction-limit value of β given in Eq. (15) and the justification is based on the strategy we employ to treat the numerical artifacts about the characteristic layers—to treat them just like the numerical artifacts about the parabolic layers in the reaction-dominant case.

8. Examples

In this section we present some examples in 2D for the CDR problem defined by Eq. (1). The domain Ω is discretized by considering both structured and unstructured meshes made up of just the bilinear block finite elements. The unstructured meshes are obtained by randomly perturbing the interior nodes of structured meshes with coordinates (x_i, y_i) as follows [55,56]:

$$x_i' = x_i + \ell_1 \delta^* \texttt{rand}(); \quad y_i' = y_i + \ell_2 \delta^* \texttt{rand}() \tag{43}$$

where, (x_i', y_i') represent the corresponding coordinates of the unstructured mesh, ℓ_1, ℓ_2 represent the mesh sizes of the structured mesh, δ^* is a mesh distortion parameter and $\texttt{rand}()$ is a function that returns random numbers uniformly distributed in the interval $[-1, 1]$. Fig. 5 illustrates two types of unstructured meshes obtained by this procedure using a 20×20 square mesh and the parameter $\delta^* = 0.2$. In Fig. 5(a), $\delta^* = 0.2$ was chosen for all the internal nodes of the mesh. Whereas for the nodes adjacent to the boundary in the mesh shown in Fig. 5(b), the perturbation perpendicular to

Box 2 Summary of the HRPG method in multi dimensions using the lowest order block finite elements and considering the generalized trapezoidal method for time integration. In the numerical examples the choice $\theta = 1/2$ is made which represents the implicit midpoint rule. δ^i_j represents the Kronecker delta.

Residual

$$R(\phi_h^{n+\theta}) := \frac{\phi_h^{n+\theta} - \phi_h^n}{\theta \Delta t} + \mathbf{u} \cdot \nabla \phi_h^{n+\theta} - \nabla \cdot \left(k \nabla \phi_h^{n+\theta}\right) + s \phi_h^{n+\theta} - f(\mathbf{x})$$

HRPG method

$$\int_\Omega w_h \frac{\phi_h^{n+\theta} - \phi_h^n}{\theta \Delta t}\, \mathrm{d}\Omega + a\left(w_h, \phi_h^{n+\theta}\right) + \sum_K \int_K (\mathbf{h} \cdot \nabla w_h) R(\phi_h^{n+\theta})\, \mathrm{d}\Omega + \sum_K \int_K \frac{|R(\phi_h^{n+\theta})|}{|\nabla \phi_h^{n+\theta}|} \left(\nabla w_h \cdot \mathbf{H} \cdot \nabla \phi_h^{n+\theta}\right) \mathrm{d}\Omega = l(w_h)$$

$$\phi_h^{n+1} = \frac{1}{\theta} \phi_h^{n+\theta} - \frac{(1-\theta)}{\theta} \phi_h^n$$

Definitions

$$a(w, \phi) := \int_\Omega w[\mathbf{u} \cdot \nabla \phi + s\phi] + k \nabla w \cdot \nabla \phi \, \mathrm{d}\Omega$$

$$l(w) := \int_\Omega w f(x)\, \mathrm{d}\Omega - \int_{\Gamma_N} w g^p \, \mathrm{d}\Gamma_N$$

$$\mathrm{J}_{ij} := \frac{\partial x_i}{\partial \widetilde{x}_j}; \quad \widetilde{\mathrm{e}}^i_j := \delta^i_j; \quad \boxed{\mathbf{l}^i := 2\mathbf{J} \cdot \widetilde{\mathbf{e}}^i}$$

$$\widehat{s}^i := \max_{j \neq i} \sqrt{2} \frac{|\mathbf{u} \cdot \mathbf{l}^j|}{|\mathbf{l}^j|^2}; \quad \gamma^i := \frac{\mathbf{u} \cdot \mathbf{l}^i}{2k}; \quad \sigma^i := \frac{s|\mathbf{l}^i|^2}{\mathbf{u} \cdot \mathbf{l}^i}; \quad \widehat{\omega}^i := \frac{\widehat{s}^i |\mathbf{l}^i|^2}{k}$$

$$\lambda^i := \frac{1}{3\left(1 + \sqrt{|\sigma^i|}\right)}; \quad \boxed{\alpha^i := \lambda^i \, \mathrm{sgn}(\mathbf{u} \cdot \mathbf{l}^i) \max\left\{\left[1 - \frac{1}{|\gamma^i|}\right], 0\right\}}$$

$$\Delta t = t^{n+1} - t^n; \quad \theta \in (0,1); \quad \overline{\delta} := \frac{1}{\theta \Delta t} \frac{\|\phi_h^{n+\theta} - \phi_h^n\|_\infty}{\|\phi_h^{n+\theta}\|_\infty}$$

$$\widetilde{u}^i := \frac{\mathbf{u} \cdot \mathbf{l}^i}{|\mathbf{l}^i|} - \frac{\alpha^i |\mathbf{l}^i| s}{2} - \frac{\alpha^i |\mathbf{l}^i| \overline{\delta}}{2}; \quad \widetilde{k}^i := k + \frac{\alpha^i \mathbf{u} \cdot \mathbf{l}^i}{2}; \quad \widetilde{s} := s + \overline{\delta}$$

$$\widetilde{\gamma}^i := \frac{|\widetilde{u}^i| |\mathbf{l}^i|}{2\widetilde{k}^i}; \quad \widetilde{\sigma}^i := \frac{\widetilde{s}|\mathbf{l}^i|}{|\widetilde{u}^i|}; \quad \widetilde{\omega}^i := \frac{\widetilde{s}|\mathbf{l}^i|^2}{\widetilde{k}^i}$$

$$\boxed{\beta^i := \max\left\{\left[\frac{2}{3}\left(\frac{\widetilde{\sigma}^i + 3}{\widetilde{\sigma}^i + 2}\right) - \left(\frac{4}{\widetilde{\omega}^i + 4\widetilde{\gamma}^i}\right)\right], \left[\frac{2}{3} - \frac{4}{\widetilde{\omega}^i}\right], 0\right\}}$$

$$\mathbf{h} := \sum_i \frac{1}{2} \alpha^i \mathbf{l}^i; \quad \mathbf{H} := \sum_i \frac{1}{2} \frac{\beta^i}{|\mathbf{l}^i|} [\mathbf{l}^i \otimes \mathbf{l}^i]$$

the boundary was set to zero. The unstructured meshes obtained using the former and later techniques are denoted as 'Type I' and 'Type II' respectively.

The linearization of the HRPG method summarized in Box 2 was done by the Picard method. The error in the nonlinear iterations was measured in the following norm:

$$\frac{\|\Phi^{i+1} - \Phi^i\|_\mathrm{e}}{\|\Phi^{i+1}\|_\mathrm{e}} \tag{44}$$

where $\|\cdot\|_\mathrm{e}$ is the standard Euclidean vector norm, Φ represents the FE nodal unknowns and i represents the iteration counter. A tolerance of 1e−5 was chosen as the termination criteria and a maximum of 20 iterations were allowed for the steady-state examples. For the transient examples the corresponding choices were 1e−3 (tolerance) and 5 (maximum iterations), respectively. The nonlinear iterations were initialized by the solution obtained by the SUPG method.

8.1. Steady-state examples

In this section we illustrate the performance of the HRPG method for the stationary CDR problem. Unless otherwise specified, in all the examples the following data is considered. The domain Ω is $[0,1] \times [0,1]$. Each example is solved using four meshes, two of which are structured and the remaining two are unstructured. The structured meshes consists of 20×20 (uniform/square) and 40×20 (rectangular) bilinear elements respectively. The unstructured meshes are obtained from the considered uniform mesh via the two perturbation techniques described earlier and illustrated in Fig. 5. The obtained solutions are illustrated as surface plots whose view is described as $(\theta^\circ, \psi^\circ)$, where θ° is the azimuthal angle with respect to the negative y-axis and ψ° is the elevation angle from the x–y plane.

Example 1. This is a classical steady-state problem introduced in [3] where the advection is skew to the mesh with downwind essential boundary conditions. The problem data is: $\mathbf{u} = (5, -9)$, $k = 10^{-8}$, $s = 0$ and $f = 0$. The boundary conditions are: $\phi = 1$ on $(x = 0, y > 0.7) \cup (x < 1, y = 1)$, $\phi = 0.5$ at $(x = 0, y = 0.7)$ and $\phi = 0$ on the rest of the boundary. This problem has exponential boundary layers at the outflow boundary and an internal characteristic layer. Fig. 6 illustrates the solutions obtained by the HRPG method viewed at (20°,20°).

Example 2. This problem was studied in [41] wherein a nonuniform rotational velocity field is employed in a rectangular domain $\Omega := [-1,1] \times [0,1]$. Structured meshes of 40×20 (uniform/square) and 80×20 (rectangular) bilinear elements are used. The unstructured meshes are obtained from the uniform mesh via the two perturbation techniques described earlier. The problem data is: $\mathbf{u} = 10^4(y[1 - x^2], -x[1 - y^2])$, $k = 10^{-4}$, $f = 0$, $s = 0$. The boundary conditions are: $\phi = 1$ on $(x < -0.5, y = 0)$, $\phi = 0.5$ at $(x = -0.5, y = 0)$, $\phi = 0$ on $(-0.5 < x \leqslant 0, y = 0) \cup (x = 1, y)$ and on the rest of the boundary the Neumann condition $\mathbf{n} \cdot \nabla \phi = 0$ is imposed. The numerical solution of the HRPG method viewed at (20°,20°) is shown in Fig. 7.

Example 3. This is a uniform advection problem with a constant source term introduced in [57]. The problem data is: $\mathbf{u} = (1, 0)$, $k = 10^{-8}$, $f = 1$, $s = 0$. The homogeneous boundary condition $\phi = 0$ is imposed everywhere. The exact solution develops exponential layers at the outlet boundary $(x = 1, y)$ and characteristic boundary layers at $(x, y = 0)$ and $(x, y = 1)$. The numerical solution of the HRPG method viewed at (−45°,20°) is shown in Fig. 8.

Example 4. This is a non-uniform advection problem with a constant source term introduced in [58]. The advection is caused by a unit angular velocity field. Structured meshes of 64×64 (uniform/square) and 128×64 (rectangular) bilinear elements are used. The unstructured meshes are obtained from the uniform mesh via the two perturbation techniques described earlier. The problem data is: $\mathbf{u} = (y, -x)$, $k = 10^{-6}$, $f = 1$, $s = 0$. The homogeneous boundary condition $\phi = 0$ is imposed everywhere. This problem has

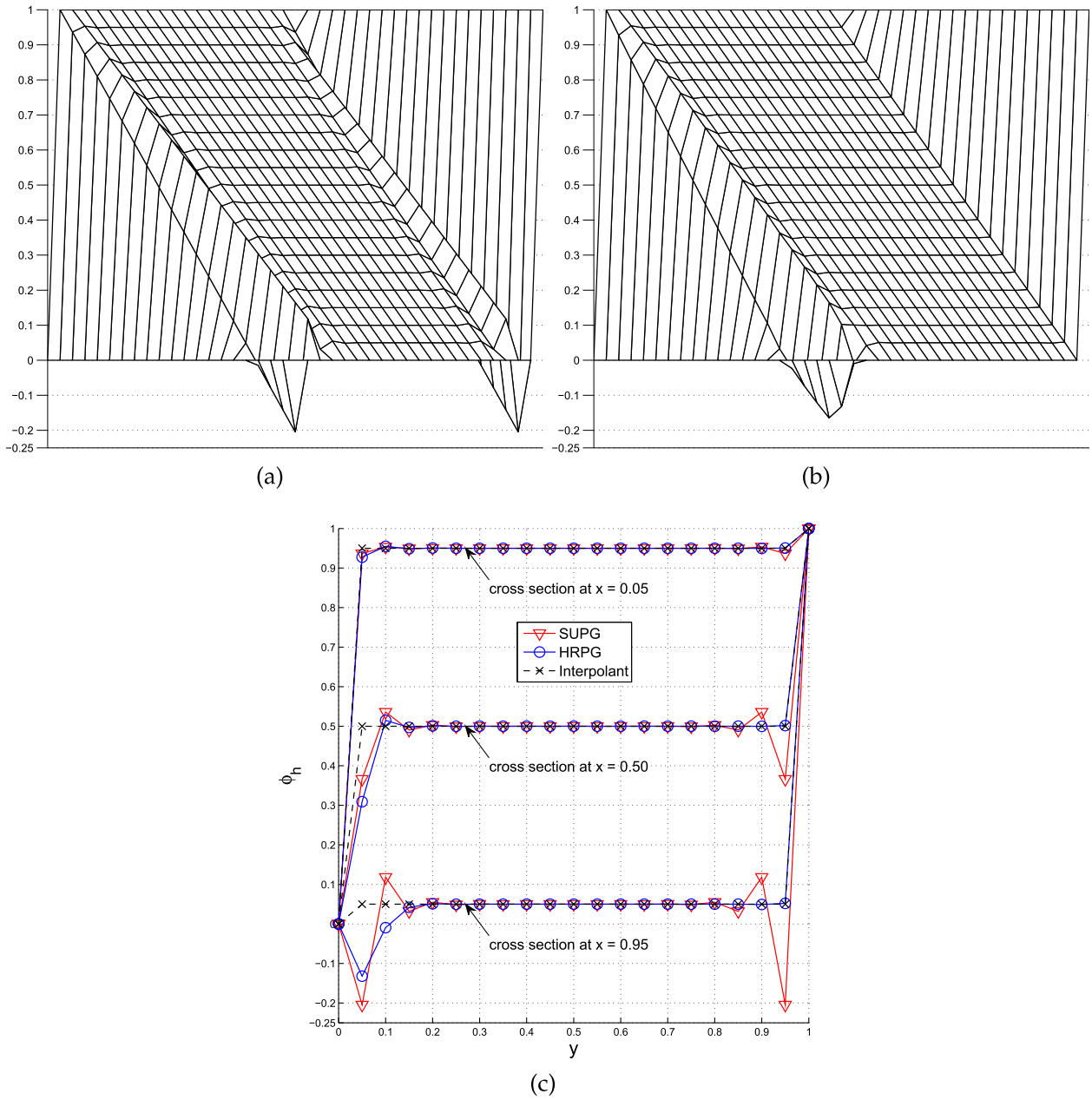

Fig. 19. Example 10, uniform advection with a negative source term. The solution obtained on a uniform 20×20 mesh viewed at $(45°,0°)$ and using (a) the SUPG method, (b) the HRPG method, (c) comparison of the nodally exact interpolant at three different cross sections with the numerical solution obtained by the SUPG and the HRPG method.

a complicated boundary layer. For instance close to the boundary $(x,y=0)$ and with an increase in x, these layers gradually vary from being parabolic to exponential while maintaining a constant profile height $\phi(x,y=0) \approx (\pi/2)$ (away from the corners). Close to the boundary $(x=1,y)$ the solution profile is approximately $\phi(x=1,y) \approx (\pi/2) - 2\tan^{-1}(y)$. The numerical solution of the HRPG method viewed at $(-200°,20°)$ is shown in Fig. 9.

Example 5. This is a uniform advection problem with a discontinuous source term introduced in [16]. The problem data is: $\mathbf{u} = (1,0)$, $k = 10^{-8}$, $f(x \leqslant 0.5,y) = 1$, $f(x > 0.5,y) = -1$, $s = 0$. The homogeneous boundary condition $\phi = 0$ is imposed everywhere. Structured meshes of 30×30 (uniform/square) and 60×30 (rectangular) bilinear elements are used. The unstructured meshes are obtained from the uniform mesh via the two perturbation techniques described earlier. The numerical solution of the HRPG method viewed at $(-10°,20°)$ is shown in Fig. 10.

Example 6. This is a plain diffusion–reaction problem. The problem data is: $\mathbf{u} = (0,0)$, $k = 10^{-8}$, $f = 1$, $s = 1$. The homogeneous boundary condition $\phi = 0$ is imposed everywhere. The numerical solution of the HRPG method viewed at $(-45°,20°)$ is shown in Fig. 11.

Example 7. This is a multidimensional modification of the CDR problem studied earlier in [41,48]. The problem data is: $\mathbf{u} = (0.01,0)$, $k = 10^{-4}$, $s = 4.8$ and $f = 0$. The boundary conditions are: $\phi = 1.0$ on $(x = 0,y) \cup (x,y = 0)$, $\phi = (3/8)$ on the rest of the boundary. The value of the element dimensionless numbers γ^1, ω^1 are *2.5* and 120 respectively. Recall that for similar problem data in 1D (cf. [48, Section 5.7.1]) the upwind numerical artifacts in the solution of Galerkin method were found to be enhanced in the solution of the SUPG method. The numerical solution of the HRPG method viewed at $(120°,20°)$ is shown in Fig. 12.

For the considered steady-state examples Table 2 lists the maximum and minimum values of the obtained HRPG solutions and

provides a comparison of the same with the corresponding values of the exact solutions. The number of nonlinear iterations required for convergence using a tolerance of 1e−2, 1e−3 and 1e−4 are also shown side by side. Just three iterations are sufficient for most of the examples should the tolerance be chosen as 1e−2.

8.2. Transient examples

Here we illustrate the performance of the HRPG method for the transient 2D pure convection problem. Only uniform bilinear finite elements are used here. Both of the examples presented here deal with the advection of solid bodies modeled with appropriate density functions. These problems are frequently used as test cases for advection algorithms demonstrating their treatment of dispersive oscillations and the overall solution accuracy.

Example 8. This is a test case introduced in the ERCOFTAC document [59]. A circular scalar bubble is initially positioned at the bottom of a square domain in a fixed constant velocity field directed at 45° toward the top right of the domain. The problem

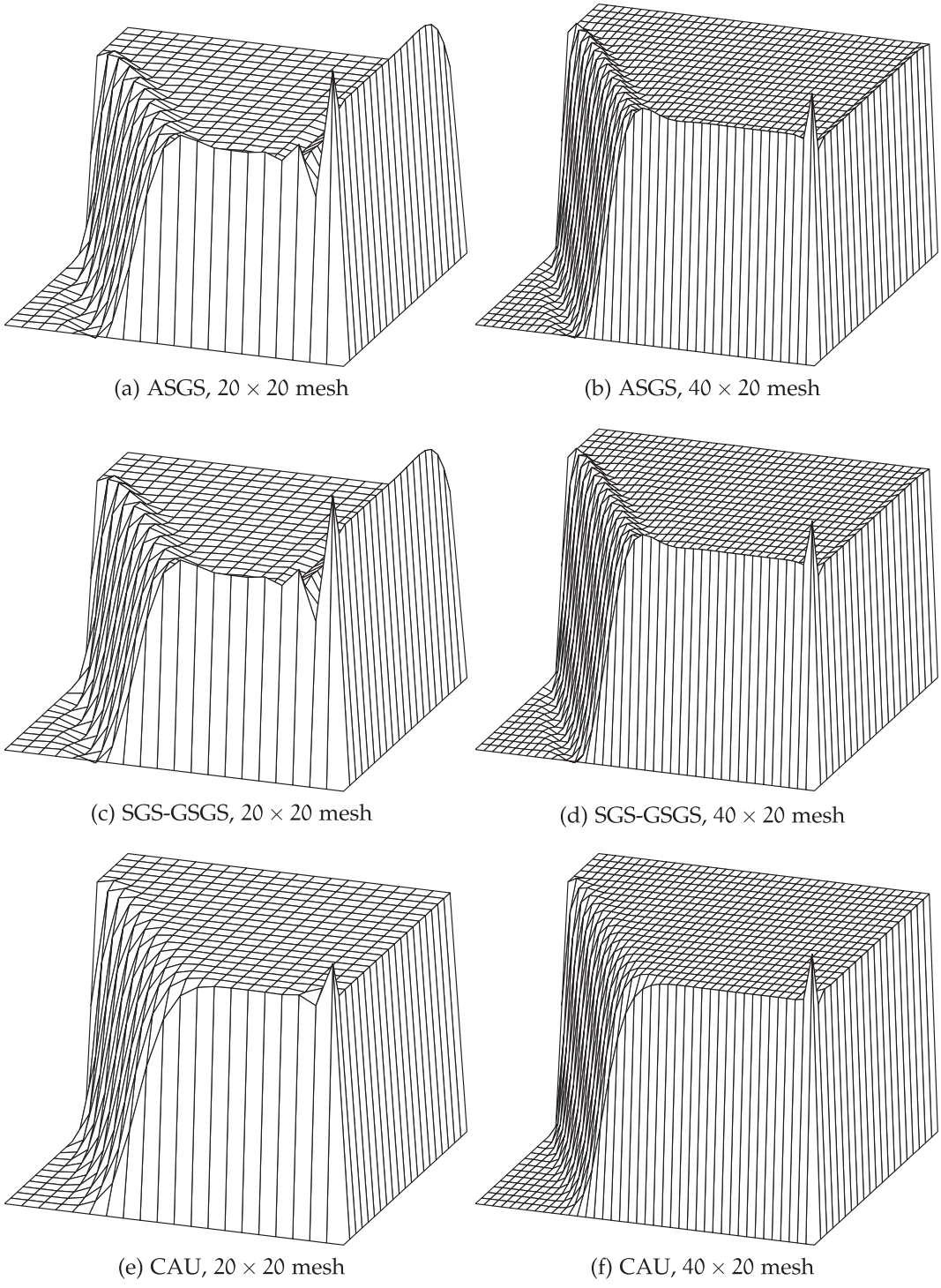

Fig. 20. Solutions to Example 1 using the ASGS [54], SGS-GSGS [40] and CAU [18] methods viewed at (20°,20°).

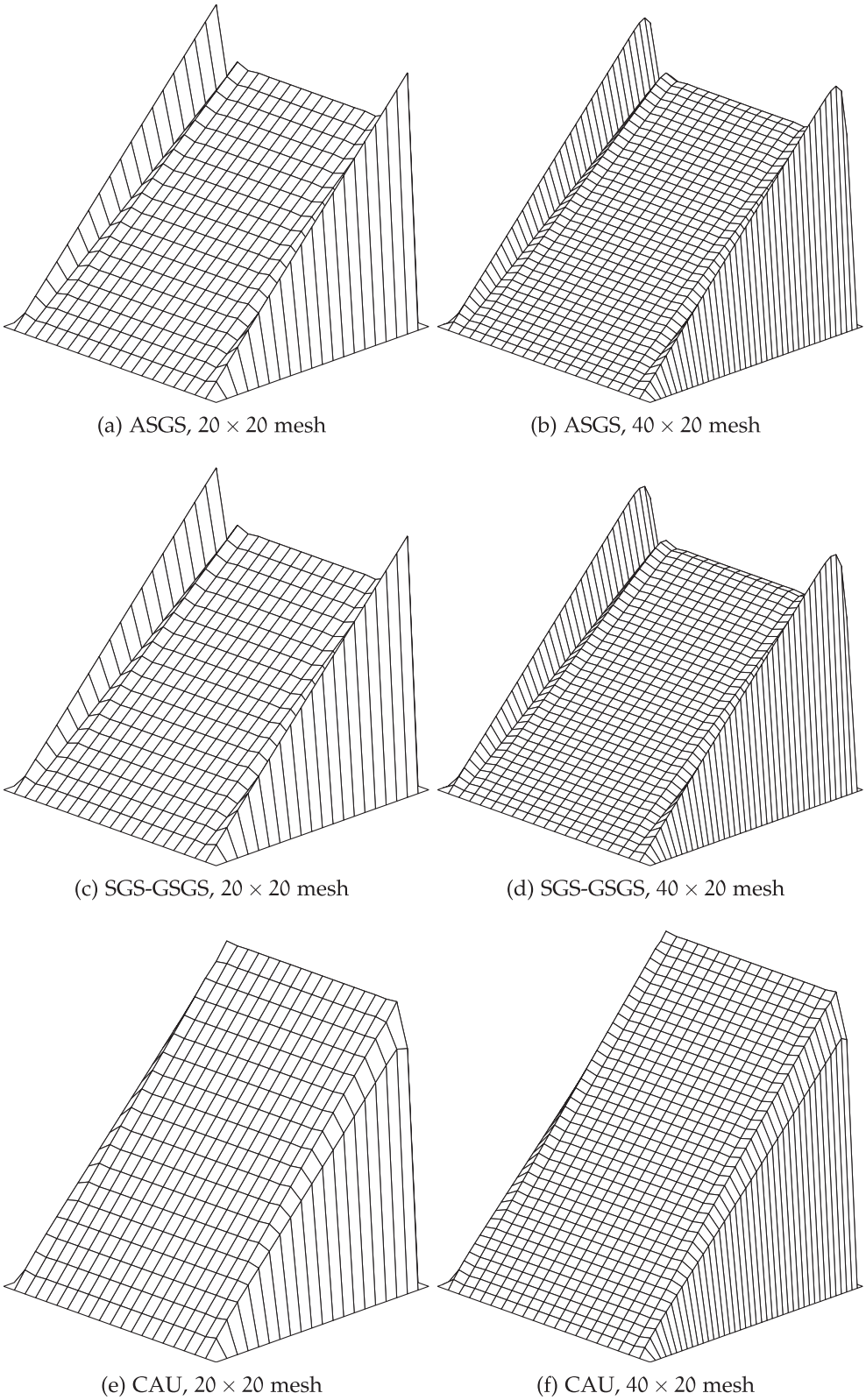

(a) ASGS, 20×20 mesh (b) ASGS, 40×20 mesh

(c) SGS-GSGS, 20×20 mesh (d) SGS-GSGS, 40×20 mesh

(e) CAU, 20×20 mesh (f) CAU, 40×20 mesh

Fig. 21. Solutions to Example 3 using the ASGS [54], SGS-GSGS [40] and CAU [18] methods viewed at $(-45°, 20°)$.

data is: $\mathbf{u} = (0.5, 0.5)$, $k = 10^{-30}$, $s = 0$ and $f = 0$. The domain $\Omega := [0,3] \times [0,3]$ is discretized by a uniform mesh of 300×300 bilinear elements. The time integration is done using the implicit midpoint rule ($\theta = 1/2$) and is advanced at a time step of 0.005 s. This corresponds to an element CFL number of 0.25. Define a radius $R = 0.25$, an arbitrary position vector $\mathbf{r} := (x, y) \in \Omega$ and a specific position vector $\mathbf{r}^c := (0.5, 0.5) \in \Omega$. The initial solution can then be expressed as follows:

$$\phi(\mathbf{r}, t = 0) = \mathrm{H}(R - |\mathbf{r} - \mathbf{r}^c|) \tag{45}$$

where H() is the Heaviside function defined earlier in Eq. (20b) and $\mathbf{r}^c$ is the center of the circular scalar bubble. The initial solution viewed at (40°,20°) is shown in Fig. 13(a) (elevation plot) and Fig. 13(c) (contour plot). The Dirichlet boundary condition $\phi = 0$ is imposed at the inlet boundaries. The numerical solution of the HRPG method at time $t \in \{1,2,3,4\}$ seconds and viewed at (40°,20°) is shown in Fig. 14 (elevation plots) and Fig. 15 (contour plots). The maximum values of the HRPG solution at the considered instances are 1.0, 1.0, 0.99999 and 0.99996, respectively. Likewise at these instances the minimum values are −9.7579e−8, −2.8204e−14, −1.7445e−20 and −5.1675e−23, respectively.

Example 9. This is a standard benchmark problem introduced in [60] that simulates the advection of a solid body subjected to a constant angular velocity field. The solid body is modeled with a scalar density function that has three shapes, viz. a slotted cylinder, a cone and a sinusoidal hump. The classical problem with just the

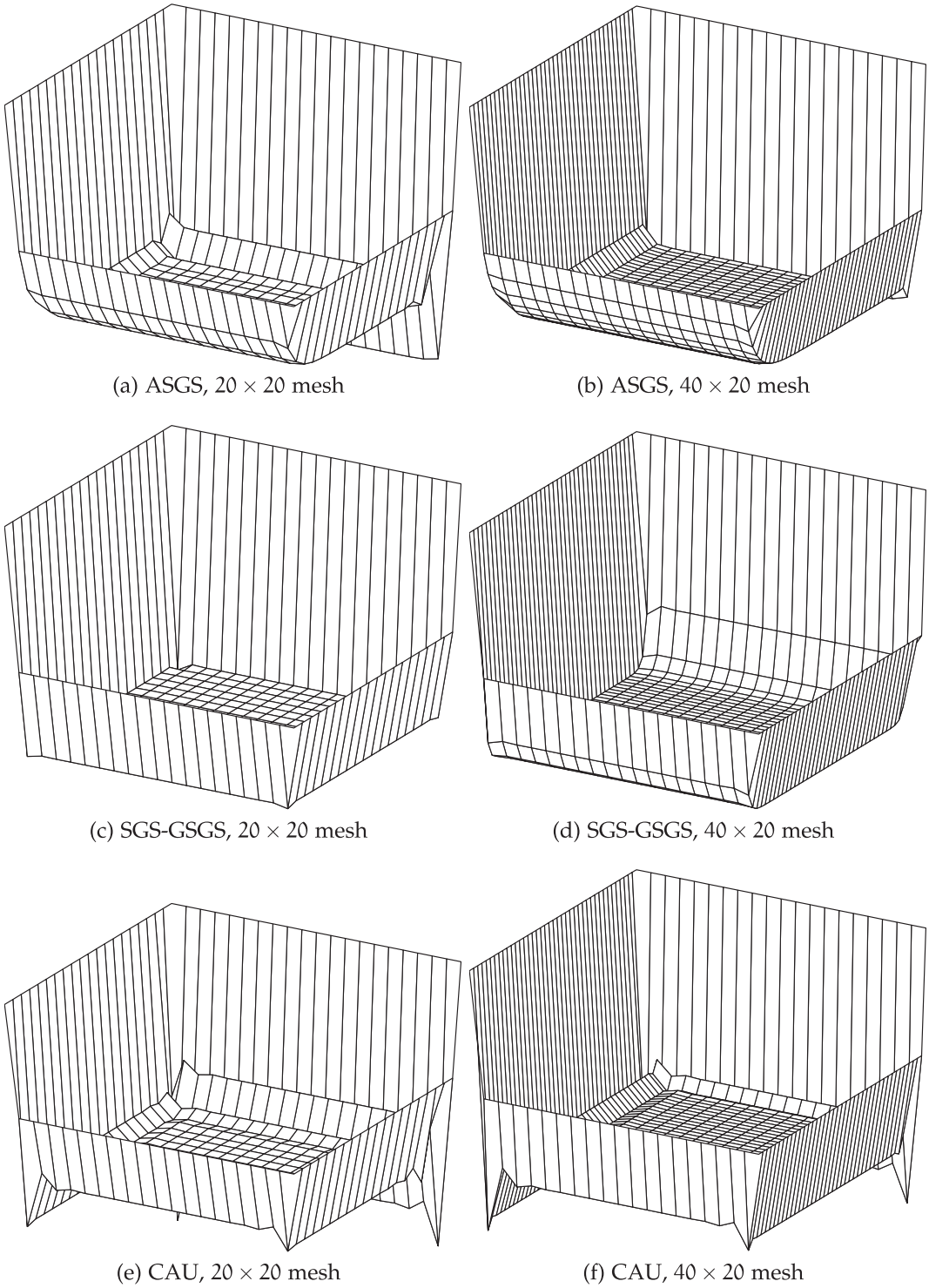

Fig. 22. Solutions to Example 7 using the ASGS [54], SGS-GSGS [40] and CAU [18] methods viewed at (120°,20°).

slotted cylinder revolving about the center of the domain was proposed by Zalesak in the seminal paper [61] that extended the FCT method to multi dimensions. The problem data is: $\mathbf{u} = (0.5 - y, x - 0.5)$, $k = 10^{-30}$, $s = 0$ and $f = 0$. The domain $\Omega := [0,1] \times [0,1]$ is discretized using 200×200 uniform bilinear elements. The time integration is done using the implicit midpoint rule ($\theta = 1/2$) and is advanced at a time step of 0.001 s. This corresponds to a maximum element CFL number of 0.1. Define a radius $R = 0.15$, an arbitrary position vector $\mathbf{r} := (x,y) \in \Omega$ and a specific position vector $\mathbf{r}^a := (x^a, y^a) \in \Omega$ for some chosen point a. The initial solution can then be expressed as follows:

$$\begin{aligned}\phi(\mathbf{r}, t = 0) &= \mathrm{H}(R - |\mathbf{r} - \mathbf{r}^1|)\left[1 - \mathrm{H}(0.025 - |x - x^1|)\mathrm{H}(0.85 - y)\right] \\ &\quad + 1 - \min\left\{\frac{|\mathbf{r} - \mathbf{r}^2|}{R}, 1\right\} \\ &\quad + \frac{1}{4}\left[1 + \cos\left(\pi \min\left\{\frac{|\mathbf{r} - \mathbf{r}^2|}{R}, 1\right\}\right)\right] \end{aligned} \tag{46}$$

where H() is the Heaviside function defined earlier in Eq. (20b), $\mathbf{r}^1 = (0.5, 0.75)$, $\mathbf{r}^2 = (0.5, 0.25)$ and $\mathbf{r}^3 = (0.25, 0.5)$ are the position vectors corresponding to the center of the slotted cylinder, the cone and the sinusoidal hump respectively. The initial solution viewed at $(-20°, 20°)$ is shown in Fig. 13(b) (elevation plot) and Fig. 13(d) (contour plot). The Dirichlet boundary condition $\phi = 0$ is imposed at the inlet boundaries. Under the considered velocity field the initial solution completes a full revolution in 2π seconds. The numerical solution of the HRPG method at time $t = \{(\pi/2), \pi, (3\pi/2), 2\pi\}$ seconds and viewed at $(-20°, 20°)$ is shown in Fig. 16 (elevation plots) and Fig. 17 (contour plots). For the considered instances in time, three different cross sections of the HRPG solution are shown in Fig. 18. With respect to Fig. 13(d), 'cut 1' represents the cross section made along the plane given by the equation $x = 0.5$. Likewise, 'cut 2' and 'cut 3' represent the cross sections given by $y = 0.5$ and $y = 0.75$. Details such as the accuracy with respect to the exact solution, the control of dispersive oscillations and the smearing of the edges in the initial solution profile can be appreciated better in these cross section plots.

8.3. Discussion

The HRPG method proposed here can be understood as the combination of upwinding plus a discontinuity-capturing operator. Also the discontinuity-capturing term has the canonical form of the shock-capturing diffusion, i.e. it is proportional to $(|\, R(\phi_h)\,| \,/\, |\, \nabla\phi_h\,|)$. Nevertheless the finer structure of the HRPG method is distinct from the existing shock-capturing Petrov–Galerkin methods in the literature (cf. Table 1). The distinction is that the upwinding provided by the characteristic tensor $\mathbf{h}$ is not streamline and the discontinuity capturing provided by the characteristic tensor $\mathbf{H}$ is neither isotropic nor purely crosswind.

It is clearly seen from the steady-state examples presented in the previous section that for structured meshes (both square and rectangular bilinear elements) the HRPG method reproduces a crisp resolution of the layers in the numerical solution. The good performance on rectangular elements (here considered with an aspect ratio of 2:1) is due to the anisotropic treatment of the stabilization terms involving the characteristic tensors $\mathbf{h}$ and $\mathbf{H}$. The solutions obtained by the HRPG method for the transient 2D advection examples advocate its good treatment of dispersive oscillations without compromising the solution-accuracy (cf. Figs. 14 and 16). Also the symmetry of the initial data is well maintained (cf. Figs. 15 and 17). Recall that the time integration was performed by the implicit midpoint rule which is a symplectic time integrator [62]. This choice was made to single-out the treatment of the geometrical symmetry in the initial data by the HRPG method.

Clearly on unstructured meshes we do not attain the same layer resolution quality as is obtained on the corresponding structured meshes. However the parabolic layers (characteristic and reactive layers) are captured satisfactorily. About the exponential layers some overshoots and undershoots are observed using Type I unstructured meshes. These unwanted localized artifacts are conspicuous in the solutions of Example 3 (Fig. 8(c)) and Example 4 (Fig. 9(c)) suggesting that there is room for further improvement of the method. Nevertheless using Type II unstructured meshes where in the random perturbation of the mesh nodes perpendicular to the domain boundary is set to zero, these unwanted artifacts about the exponential layers are greatly reduced.

Fig. 10 illustrates another shortcoming of the HRPG method that is conspicuous even when structured meshes are used. On one half of the domain (here the source term is positive) the obtained solutions have crisp layer resolutions, whereas in the remaining half (here the source term is negative) the numerical solution appears to be over-damped and even negative near the corners of the outlet boundary. This is a shortcoming suffered by all the shock-capturing techniques designed within the Petrov–Galerkin framework (see Codina's monograph [63]) that rely on the canonical strategy of adding a positive shock-capturing diffusion. The following example illustrates why the aforesaid strategy fails to address this shortcoming.

Example 10. Consider a unit domain $\Omega := [0,1] \times [0,1]$ and the following problem data: $\mathbf{u} = (1,0)$, $k = 10^{-8}$, $s = 0$ and $f = -1$. The Dirichlet boundary conditions are: $\phi = 1$ on $(x = 0, y > 0) \cup (x, y = 1)$ and $\phi = 0$ on the rest of the boundary. The domain Ω is discretized using a structured mesh of 20×20 (uniform/square) bilinear elements. In the interior of the domain the exact solution has the profile of a flat surface with a slope of -1. Along the boundaries $(x, y = 0)$ and $(x, y = 1)$ the exact solution develops characteristic boundary layers and as a consequence within the width of these characteristic layers and near the corners of the outlet boundary $(x = 1, y)$, exponential layers are formed. Hence the solution of the plain Galerkin FEM will be corrupted with global oscillations. The solutions obtained by the SUPG and the HRPG method are shown in Fig. 19.

Note that the undershoots and overshoots in the solution of the SUPG method are identical across both characteristic layers (cf. Fig. 19(a) and (c)). This is in agreement with the reasoning made in Section 4 related to the numerical artifacts across characteristic layers, i.e. unlike in the reaction-dominant case where it is the numerical solution that undergoes the 1D mass type averaging, in the convection-dominant case it is the derivatives of the numerical solution that undergo the same. Thus, the Gibbs phenomenon across the characteristic layers in the later case is proportional to the variations in the derivatives of the solution across these layers. In other words for the current problem it is the slope of ϕ_h and not the actual value of ϕ_h on the boundary that determines the observed artifacts. It can be clearly seen in Fig. 19(c) that any method, that relies on the canonical strategy of adding a *positive* shock-capturing diffusion, will not be able to recover (near the boundary $(x, y = 0)$) the nodally exact interpolant from the initial SUPG solution. On the other hand, note that the artifacts near the boundary $(x, y = 1)$ have a profile similar to the one that would have been observed for the L^2 projection of the exact solution onto the finite element space. It is for this reason that the aforesaid strategy succeeds in capturing these layers.

Obviously tailor-made solutions exist to treat this shortcoming. For instance, one such trick that recovers crisp resolution of these layers for the HRPG method and for the current problem (Example 10) is to reverse the sign of the stabilization parameter β (along the y-axis) for all elements containing the boundary section $(x, y = 0)$, thus enforcing a *negative* shock-capturing diffusion for these

elements. Unfortunately it is difficult to generalize these tailor-made tricks to an arbitrary situation. An alternative would be to change the strategy to the one which directly treats the cause of the Gibbs phenomenon for both the reactive and characteristic layers[4]—Design the weights of a Petrov–Galerkin FEM such that the typical 1D mass type averaging in the Galerkin FEM (cf. Eq. (18)) be lumped in the regions across the layers. Research in this line is still under development and we delay its introduction to future works.

Remark 6. Fortunately, this idea which was born to treat this shortcoming in the CDR problem, has opened door to a class of higher-order compact Petrov–Galerkin FEM effective for the Helmholtz problem. The design of such a Petrov–Galerkin FEM and its applications to the Helmholtz equation is the subject matter of the paper [64].

8.4. Comparison with other methods

Here we make a comparison of the solutions obtained using the HRPG method with those obtained using the ASGS [54], SGS-GSGS [40] and CAU [18] methods. To be precise, we compare three steady state examples, viz. Examples 1, 3 and 7. These examples are solved on structured meshes only and are illustrated in Figs. 20–22, respectively.

Note that the ASGS and SGS-GSGS methods are linear methods proposed for the CDR problem. The ASGS method is a single-parameter method wherein this scalar stabilization parameter was designed to attain a robust method (with respect to global stability) even on anisotropic meshes. In the advective limit the SGS-GSGS method recovers the SGS method [11]. Thus, in this case the solutions of the ASGS and SGS-GSGS methods will be similar. As shock-capturing is not a design objective, these methods will yield local instabilities in the presence of sharp layers (cf. Fig. 20(a)–(d), Fig. 21(a)–(d), Fig. 22(a)–(d)).

When high element advection (large γ) is combined with strong element reaction (large ω), the local instabilities that appear in the Galerkin method are occasionally enhanced in several linear single-parameter stabilized methods [39–41,48]. The SGS-GSGS method is a two-parameter method designed to treat these local instabilities in the presence of strong element reaction. This improvement over the ASGS method (cf. Fig. 22(a)) can be seen in Fig. 22(c). As the maximum element size is used to calculate the stabilization parameters in the SGS-GSGS method, we get a smeared solution on a rectangular mesh (cf. Fig. 21(d) and Fig. 22(d)).

On the other hand, shock-capturing is a design objective for the CAU method which is nonlinear. Fig. 20(e) and (f), Fig. 21(e) and (f) illustrate that the local instabilities found in the ASGS and SGS-GSGS methods are greatly controlled by the CAU method in Examples 1 and 3. Recall that, unlike some other shock-capturing methods (e.g. [17,21]), the CAU method retains the shock-capturing terms even in 1D and in several limit cases of the CDR problem [48]. However, the expressions of the stabilization parameters were never optimized for these limit cases. Thus, there are instances when the CAU method is either over-diffusive (cf. Fig. 21(e) and (f)) or fails to improve upon the initial solution obtained by the SUPG method (cf. Fig. 22(e) and (f)). Such lack of improvement upon the initial SUPG solution has been observed even in 1D [48]. The improvement in the accuracy and layer resolution obtained by the HRPG method for the considered examples are evident in Figs. 6(a) and (b), Fig. 8(a) and (b), Fig. 12(a) and (b). However, for the considered examples, the HRPG method needed one or two iterations more than the CAU method.

[4] This idea is a fruit of the discussions with Prof. Ramon Codina.

9. Conclusions

We have developed a multi dimensional extension of the HRPG method presented earlier in [48] for the 1D CDR problem. As the characteristic internal/boundary layers found in the convection-dominant case are a unique feature of the solution in higher dimensions, they do not have any counterparts in 1D. Hence, a straight-forward extension of the stabilization parameters of the HRPG method derived for the 1D case will not be efficient to resolve these parabolic layers.

The numerical artifacts that are formed across the parabolic layers are usually manifested as the Gibbs phenomenon. The strategy we employ to treat the artifacts about the characteristic layers is to treat them just like the artifacts found across the parabolic layers in the reaction-dominant case. This is done by relating the characteristic layers in the convection–diffusion problem to the parabolic layers formed in a fictitious diffusion–reaction problem. The fictitious reaction coefficient in the later problem is designed such that the parabolic layers in both the problems have the same width. Using this fictitious reaction coefficient, we present a nondimensional element number that quantifies these characteristic layers. By quantification we mean that it should serve a similar purpose in the definition of the stabilization parameters as the element Peclet number does for the exponential layers.

Although the structure of HRPG method in 1D is identical to the consistent approximate upwind Petrov–Galerkin method [18], in multi dimensions the former method has a unique structure. The distinction is that in general the upwinding is not streamline and the discontinuity-capturing is neither isotropic nor purely cross-wind. In this line, we present anisotropic element length vectors $\mathbf{l}^i$ and using them objective characteristic tensors associated with the HRPG method are defined. Only the multilinear block finite elements are considered in this study. Except for the modification to include the new dimensionless number that quantifies the characteristic layers, the definition of the stabilization parameters α^i,β^i calculated along the element length vectors $\mathbf{l}^i$ are a direct extension of their counterparts in 1D summarized earlier in [48, Section 5.6].

Finally, several steady-state and transient examples are presented that throw light on the good performance of the proposed method.

An extension of the HRPG formulation within the finite calculus (FIC) framework to the study of convection–diffusion–absorption problems using linear triangles can be found in [65].

Acknowledgments

The first author acknowledges the economic support received through the FI pre-doctoral grant from the Department of Universities, Research and Information Society (Generalitat de Catalunya) and the European Social Fund. He also thanks Prof. Ramon Codina for many useful discussions.

This work was partially supported by the SAFECON project of the European Research Council (European Commission) and AIDMAR (Ref: CTM2008-06565-C03-01) of the Ministery of Science and Innovation (Spain).

References

[1] M. Stynes, Steady-state convection–diffusion problems, Acta Numerica 14 (2005) 445–508, doi:10.1017/S0962492904000261. <http://www.journals.cambridge.org/abstract_S0962492904000261> .

[2] T.J.R. Hughes, A.N. Brooks, A Theoretical Framework for Petrov–Galerkin Methods with Discontinuous Weighting Functions: Application to the

Streamline Upwind Procedure, in: R. Gallagher, D. Norrie, J. Oden, O.C. Zienkiewicz (Eds.), Finite Elements in Fluids, vol. IV, John Wiley and Sons Ltd., Chichester, 1982, pp. 47–65.
[3] A.N. Brooks, T.J.R. Hughes, Streamline upwind/Petrov–Galerkin formulations for convection dominated flows with particular emphasis on the incompressible Navier–Stokes equations, Comput. Methods Appl. Mech. Engrg. 32 (1–3) (1982) 199–259, doi:10.1016/0045-7825(82)90071-8. <http://linkinghub.elsevier.com/retrieve/pii/0045782582900718> .
[4] J. Donea, A Taylor–Galerkin method for convective transport problems, Int. J. Numer. Methods Engrg. 20 (1) (1984) 101–119, doi:10.1002/nme.1620200108. <http://doi.wiley.com/10.1002/nme.1620200108> .
[5] J. Douglas Jr., T.F. Russell, Numerical methods for convection-dominated diffusion problems based on combining the method of characteristics with finite element or finite difference procedures, SIAM J. Numer. Anal. 19 (5) (1982) 871, doi:10.1137/0719063. <http://link.aip.org/link/SJNAAM/v19/i5/p871/s1&Agg=doi> .
[6] R. Löhner, K. Morgan, O.C. Zienkiewicz, The solution of non-linear hyperbolic equation systems by the finite element method, Int. J. Numer. Methods Fluids 4 (11) (1984) 1043–1063, doi:10.1002/fld.1650041105. <http://doi.wiley.com/10.1002/fld.1650041105> .
[7] T.J.R. Hughes, L.P. Franca, G.M. Hulbert, A new finite element formulation for computational fluid dynamics: VIII. The Galerkin/least-squares method for advective–diffusive equations, Comput. Methods Appl. Mech. Engrg. 73 (1989) 173–189, doi:10.1016/0045-7825(89)90111-4.
[8] F. Brezzi, M.-O. Bristeau, L.P. Franca, M. Mallet, G. Rogé, A relationship between stabilized finite element methods and the Galerkin method with bubble functions, Comput. Methods Appl. Mech. Engrg. 96 (1) (1992) 117–129, doi:10.1016/0045-7825(92)90102-P. <http://linkinghub.elsevier.com/retrieve/pii/004578259290102P> .
[9] C. Baiocchi, F. Brezzi, L.P. Franca, Virtual bubbles and Galerkin-least-squares type methods (Ga.L.S.), Comput. Methods Appl. Mech. Engrg. 105 (1) (1993) 125–141, doi:10.1016/0045-7825(93)90119-I. <http://linkinghub.elsevier.com/retrieve/pii/004578259390119I> .
[10] F. Brezzi, A. Russo, Choosing bubbles for advection–diffusion problems, Math. Models Methods Appl. Sci. 4 (4) (1994) 571–587.
[11] T.J.R. Hughes, Multiscale phenomena: Green's functions, the Dirichlet-to-Neumann formulation, subgrid scale models, bubbles and the origins of stabilized methods, Comput. Methods Appl. Mech. Engrg. 127 (1–4) (1995) 387–401, doi:10.1016/0045-7825(95)00844-9. <http://linkinghub.elsevier.com/retrieve/pii/0045782595008449> .
[12] T.J.R. Hughes, G.R. Feijóo, L. Mazzei, J.-B. Quincy, The variational multiscale method – A paradigm for computational mechanics, Comput. Methods Appl. Mech. Engrg. 166 (1–2) (1998) 3–24, doi:10.1016/S0045-7825(98)00079-6. <http://linkinghub.elsevier.com/retrieve/pii/S0045782598000796> .
[13] O.C. Zienkiewicz, R. Codina, A general algorithm for compressible and incompressible flow – Part I. the split, characteristic-based scheme, Int. J. Numer. Methods Fluids 20 (8–9) (1995) 869–885, doi:10.1002/fld.1650200812. <http://doi.wiley.com/10.1002/fld.1650200812> .
[14] E. Oñate, Deriva tion of stabilized equations for numerical solution of advective–diffusive transport and fluid flow problems, Comput. Methods Appl. Mech. Engrg. 151 (1–2) (1998) 233–265, doi:10.1016/S0045-7825(97)00119-9. <http://linkinghub.elsevier.com/retrieve/pii/S0045782597001199> .
[15] R. Codina, Comparison of some finite element methods for solving the diffusion–convection–reaction equation, Comput. Methods Appl. Mech. Engrg. 156 (1–4) (1998) 185–210, doi:10.1016/S0045-7825(97)00206-5.
[16] A. Mizukami, T.J.R. Hughes, A Petrov–Galerkin finite element method for convection-dominated flows: an accurate upwinding technique for satisfying the maximum principle, Comput. Methods Appl. Mech. Engrg. 50 (2) (1985) 181–193, doi:10.1016/0045-7825(85)90089-1. <http://linkinghub.elsevier.com/retrieve/pii/0045782585900891> .
[17] T.J.R. Hughes, M. Mallet, A. Mizukami, A new finite element formulation for computational fluid dynamics: II. Beyond SUPG, Comput. Methods Appl. Mech. Engrg. 54 (3) (1986) 341–355, doi:10.1016/0045-7825(86)90110-6. <http://linkinghub.elsevier.com/retrieve/pii/0045782586901106> .
[18] A.C. Galeão, E.G.D. do Carmo, A consistent approximate upwind Petrov–Galerkin method for convection-dominated problems, Comput. Methods Appl. Mech. Engrg. 68 (1) (1988) 83–95, doi:10.1016/0045-78259(88)90108-9. <http://linkinghub.elsevier.com/retrieve/pii/0045782588901089> .
[19] C. Johnson, A. Szepessy, P. Hansbo, On the convergence of shock-capturing streamline diffusion finite element methods for hyperbolic conservation laws, Math. Comput. 54 (189) (1990) 107–129. <http://www.jstor.org/stable/2008684> .
[20] E.G.D. do Carmo, A.C. Galeão, Feedback Petrov–Galerkin methods for convection-dominated problems, Comput. Methods Appl. Mech. Engrg. 88 (1) (1991) 1–16, doi:10.1016/0045-7825(91)90231-T. <http://linkinghub.elsevier.com/retrieve/pii/004578259190231T> .
[21] R. Codina, A discontinuity-capturing crosswind-dissipation for the finite element solution of the convection–diffusion equation, Comput. Methods Appl. Mech. Engrg. 110 (3–4) (1993) 325–342, doi:10.1016/0045-7825(93)90213-H. <http://linkinghub.elsevier.com/retrieve/pii/004578259390213H> .
[22] R. Codina, A shock-capturing anisotropic diffusion for the finite element solution of the diffusion–convection–reaction equation, in: K. Morgan, E. Oñate, J. Périaux, J. Peraire, O.C. Zienkiewicz (Eds.), Finite Elements in Fluids: New Trends and Applications, vol. 1, CIMNE, Barcelona, 1993, pp. 67–75.
[23] P.A.B. de Sampaio, A.L.G.A. Coutinho, A natural derivation of discontinuity capturing operator for convection–diffusion problems, Comput. Methods Appl. Mech. Engrg. 190 (46–47) (2001) 6291–6308, doi:10.1016/S0045-7825(01)00229-8. <http://linkinghub.elsevier.com/retrieve/pii/S0045782501002298> .
[24] E. Burman, A. Ern, Nonlinear diffusion and discrete maximum principle for stabilized Galerkin approximations of the convection–diffusion–reaction equation, Comput. Methods Appl. Mech. Engrg. 191 (35) (2002) 3833–3855, doi:10.1016/S0045-7825(02)00318-3. <http://linkinghub.elsevier.com/retrieve/pii/S0045782502003183> .
[25] E.G.D. do Carmo, G.B. Alvarez, A new stabilized finite element formulation for scalar convection–diffusion problems: the streamline and approximate upwind/Petrov–Galerkin method, Comput. Methods Appl. Mech. Engrg. 192 (31–32) (2003) 3379–3396, doi:10.1016/S0045-7825(03)00292-5. <http://linkinghub.elsevier.com/retrieve/pii/S0045782503002925> .
[26] E.G.D. do Carmo, G.B. Alvarez, A new upwind function in stabilized finite element formulations, using linear and quadratic elements for scalar convection–diffusion problems, Comput. Methods Appl. Mech. Engrg. 193 (23–26) (2004) 2383–2402, doi:10.1016/j.cma.2004.01.015. <http://linkinghub.elsevier.com/retrieve/pii/S004578250400088X> .
[27] P. Knobloch, Improvements of the Mizukami–Hughes method for convection–diffusion equations, Comput. Methods Appl. Mech. Engrg. 196 (1–3) (2006) 579–594, doi:10.1016/j.cma.2006.06.004. <http://linkinghub.elsevier.com/retrieve/pii/S0045782506001964> .
[28] E. Oñate, F. Zarate, S.R. Idelsohn, Finite element formulation for convective–diffusive problems with sharp gradients using finite calculus, Comput. Methods Appl. Mech. Engrg. 195 (13–16) (2006) 1793–1825, doi:10.1016/j.cma.2005.05.036. <http://linkinghub.elsevier.com/retrieve/pii/S0045782505003075> .
[29] V. John, P. Knobloch, On spurious oscillations at layers diminishing (SOLD) methods for convection–diffusion equations: Part I – A review, Comput. Methods Appl. Mech. Engrg. 196 (17–20) (2007) 2197–2215, doi:10.1016/j.cma.2006.11.013. <http://linkinghub.elsevier.com/retrieve/pii/S0045782506003926> .
[30] T. Tezduyar, Y. Park, Discont inuity-capturing finite element formulations for nonlinear convection–diffusion–reaction equations, Comput. Methods Appl. Mech. Engrg. 59 (3) (1986) 307–325, doi:10.1016/0045-7825(86)90003-4. <http://linkinghub.elsevier.com/retrieve/pii/0045782586900034> .
[31] S.R. Idelsohn, N. Nigro, M. Storti, G. Buscaglia, A Petrov–Galerkin formulation for advection–reaction–diffusion problems, Comput. Methods Appl. Mech. Engrg. 136 (1–2) (1996) 27–46, doi:10.1016/0045-7825(96)01008-0. <http://linkinghub.elsevier.com/retrieve/pii/0045782596010080> .
[32] L.P. Franca, E.G.D. do Carmo, The Galerkin gradient least-squares method, Comput. Methods Appl. Mech. Engrg. 74 (1) (1989) 41–54, doi:10.1016/0045-7825(89)90085-6. <http://linkinghub.elsevier.com/retrieve/pii/0045782589900856> .
[33] I. Harari, T.J.R. Hughes, Stabili zed finite element methods for steady advection–diffusion with production, Comput. Methods Appl. Mech. Engrg. 115 (1–2) (1994) 165–191, doi:10.1016/0045-7825(94)90193-7. <http://linkinghub.elsevier.com/retrieve/pii/0045782594901937> .
[34] L.P. Franca, C. Farhat, Bubble functions prompt unusual stabilized finite element methods, Comput. Methods Appl. Mech. Engrg. 123 (1–4) (1995) 299–308, doi:10.1016/0045-7825(94)00721-X. <http://linkinghub.elsevier.com/retrieve/pii/004578259400721X> .
[35] L.P. Franca, F. Valentin, On an improved unusual stabilized finite element method for the advective–reactive–diffusive equation, Comput. Methods Appl. Mech. Engrg. 190 (13–14) (2000) 1785–1800, doi:10.1016/S0045-782(00)00190-0. <http://linkinghub.elsevier.com/retrieve/pii/S0045782500001900> .
[36] F. Brezzi, G. Hauke, L.D. Marini, G. Sangalli, Link-cutting bubbles for the stabilization of convection–diffusion–reaction problems, Math. Models Methods Appl. Sci. 13 (3) (2003) 445–461.
[37] R. Codina, On stabilized finite element methods for linear systems of convection–diffusion–reaction equations, Comput. Methods Appl. Mech. Engrg. 188 (1–3) (2000) 61–82, doi:10.1016/S0045-7825(00)00177-8. <http://linkinghub.elsevier.com/retrieve/pii/S0045782500001778> .
[38] G. Hauke, A. García-Olivares, Variational subgrid scale formulations for the advection–diffusion–reaction equation, Comput. Methods Appl. Mech. Engrg. 190 (51–52) (2001) 6847–6865, doi:10.1016/S0045-7825(01)00262-6. <http://linkinghub.elsevier.com/retrieve/pii/S0045782501002626> .
[39] G. Hauke, A simple subgrid scale stabilized method for the advection–diffusion–reaction equation, Comput. Methods Appl. Mech. Engrg. 191 (27–28) (2002) 2925–2947, doi:10.1016/S0045-7825(02)00217-7. <http://linkinghub.elsevier.com/retrieve/pii/S0045782502002177> .
[40] G. Hauke, G. Sangalli, M.H. Doweidar, Combining adjoint stabilized methods for the advection–diffusion–reaction problem, Math. Models Methods Appl. Sci. 17 (2) (2007) 305–326.
[41] E. Oñate, J. Miquel, G. Hauke, Stabilized formulation for the advection–diffusion–absorption equation using finite calculus and linear finite elements, Comput. Methods Appl. Mech. Engrg. 195 (33–36) (2006) 3926–3946, doi:10.1016/j.cma.2005.07.020. <http://linkinghub.elsevier.com/retrieve/pii/S0045782505003877> .
[42] E. Oñate, J. Miquel, F. Zarate, Stabilized solution of the multidimensional advection–diffusion–absorption equation using linear finite elements, Comput. Fluids 36 (1) (2007) 92–112, doi:10.1016/j.compfluid.2005.07.003. <http://linkinghub.elsevier.com/retrieve/pii/S0045793005001313> .

[43] C.A. Felippa, E. Oñate, Nodally exact Ritz discretizations of 1D diffusion–absorption and Helmholtz equations by variational FIC and modified equation methods, Comput. Mech. 39 (2) (2007) 91–111, doi:10.1007/s00466-005-0011-z. <http://www.springerlink.com/index/10.1007/s00466-005-0011-z> .
[44] I. Harari, Stability of semidiscrete formulations for parabolic problems at small time steps, Comput. Methods Appl. Mech. Engrg. 193 (15–16) (2004) 1491–1516, doi:10.1016/j.cma.2003.12.035. <http://linkinghub.elsevier.com/retrieve/pii/S0045782504000465> .
[45] I. Harari, G. Hauke, Semidiscrete formulations for transient transport at small time steps, Int. J. Numer. Methods Fluids 54 (6–8) (2007) 731–743, doi:10.1002/fld.1487. <http://doi.wiley.com/10.1002/fld.1487> .
[46] S.R. Idelsohn, J.C. Heinrich, E. Oñate, Petrov–Galerkin methods for the transient advective–diffusive equation with sharp gradients, Int. J. Numer. Methods Engrg. 39 (9) (1996) 1455–1473, doi:10.1002/(SICI)1097-0207(19960515)39:9<1455::AID-NME912>3.0.CO;2-0. <http://doi.wiley.com/10.1002/%28SICI%291097-0207%2819960515%2939%3A9%3C1455%3A%3AAID-NME912%3E3.0.CO%3B2-0> .
[47] C.-C. Yu, J.C. Heinrich, Petrov–Galerkin methods for the time-dependent convective transport equation, Int. J. Numer. Methods Engrg. 23 (5) (1986) 883–901, doi:10.1002/nme.1620230510 <http://doi.wiley.com/10.1002/nme.1620230510> .
[48] P. Nadukandi, E. Oñate, J. García, A high-resolution Petrov–Galerkin method for the 1D convection–diffusion–reaction problem, Comput. Methods Appl. Mech. Engrg. 199 (9–12) (2010) 525–546, doi:10.1016/j.cma.2009.10.009. <http://linkinghub.elsevier.com/retrieve/pii/S0045782509003545> .
[49] P. Nadukandi, Stabilized finite element methods for convection–diffusion–reaction, Helmholtz and Stokes problems, Ph.D. thesis, Universitat Politècnica de Catalunya, 2011.
[50] D. Kuzmin, R. Löhner, S. Turek, Flux-Corrected Transport: Principles, Algorithms and Applications, Springer, 2005.
[51] J. Kevorkian, Matched Asymptotic Expansions, in: Partial Differential Equations: Analytical Solution Techniques, second ed., Springer-Verlag, 1999. Chapter 8.2.
[52] G. Strang, Diffusion, Convection, and Finance, in: Computational Science and Engineering, first ed., Wellesley-Cambridge Press, 2007. Chapter 6.5. <http://math.mit.edu/cse/> .
[53] C.-C. Yu, J.C. Heinrich, Petrov–Galerkin method for multidimensional, time-dependent, convective-diffusion equations, Int. J. Numer. Methods Engrg. 24 (11) (1987) 2201–2215, doi:10.1002/nme.1620241112. <http://doi.wiley.com/10.1002/nme.1620241112> .
[54] J. Principe, R. Codina, On the stabilization parameter in the subgrid scale approximation of scalar convection–diffusion–reaction equations on distorted meshes, Comput. Methods Appl. Mech. Engrg. 199 (21–22) (2010) 1386–1402, doi:10.1016/j.cma.2009.08.011. <http://linkinghub.elsevier.com/retrieve/pii/S0045782509002564> .
[55] A.F.D. Loula, D.T. Fernandes, A quasi optimal Petrov–Galerkin method for Helmholtz problem, Int. J. Numer. Methods Engrg. 80 (12) (2009) 1595–1622, doi:10.1002/nme.2677. <http://doi.wiley.com/10.1002/nme.2677> .
[56] D.T. Fernandes, A.F.D. Loula, Quasi optimal finite difference method for Helmholtz problem on unstructured grids, Int. J. Numer. Methods Engrg. 82 (2009) 1244–1281, doi:10.1002/nme.2795. <http://doi.wiley.com/10.1002/nme.2795> .
[57] F. Kikuchi, T. Ushijima, Theoretical analysis of some finite element schemes for convective diffusion equations, in: R. Gallagher, D. Norrie, J. Oden, O.C. Zienkiewicz (Eds.), Finite Elements in Fluids, vol. IV, John Wiley and Sons Ltd, Chichester, 1982.
[58] J. Xu, L. Zikatanov, A monotone finite element scheme for convection–diffusion equations, Math. Comput. 68 (228) (1999) 1429–1447, doi:10.1090/S0025-5718-99-01148-5. <http://www.ams.org/journal-getitem?pii=S0025-5718-99-01148-5> .
[59] M. Casey, T. Wintergerste (Eds.), ERCOFTAC best practice guidelines for Industrial Computational Fluid Dynamics, Ercoftac, Brussels, 2000.
[60] R.J. LeVeque, High-resolution conservative algorithms for advection in incompressible flow, SIAM J. Numer. Anal. 33 (2) (1996) 627–665, doi:10.1137/0733033. <http://link.aip.org/link/SJNAAM/v33/i2/p627/s1&Agg=doi>.
[61] S.T. Zalesak, Fully multidimensional flux-corrected transport algorithms for fluids, J. Comput. Phys. 31 (3) (1979) 335–362, doi:10.1016/0021-9991(79)90051-2. <http://linkinghub.elsevier.com/retrieve/pii/0021999179900512> .
[62] E. Hairer, C. Lubich, G. Wanner, Geometric numerical integration: structure-preserving algorithms for ordinary differential equations, Springer Series in Computational Mathematics, vol. 31, Springer-Verlag, Berlin/Heidelberg, 2006. <http://www.springerlink.com/index/10.1007/3-540-30666-8> .
[63] R. Codina, A finite element formulation for the numerical solution of the convection–diffusion equation, first edition, CIMNE, Barcelona, 1993. <http://www.cimne.com/tiendaCIMNE/ProductosCon.asp?id_prod=56>.
[64] P. Nadukandi, E. Oñate, J. García, A Petrov–Galerkin formulation for the alpha-interpolation of FEM and FDM stencils. Applications to the Helmholtz equation, Int. J. Numer. Methods Engrg., in press, doi:10.1002/nme.3291.
[65] E. Oñate, J. Miquel, P. Nadukandi, A stable and accurate finite element formulation for convection–diffusion–absorption problem using finite calculus, Research Report PI 352, CIMNE, Barcelona, March 2011.